
TECHNISCHE UNIVERSITÄT WIEN
Vienna University of Technology

Master Thesis

# Feasibility of CBCT-based dose calculation for adaptive radiotherapy: comparison of three HU adjustment techniques

Thomas Steininger, BSc.

Geistingergasse 1/7/5

A-1190 Vienna

August 25, 2011

Supervisor:

Univ.-Doz. Dipl.-Ing. Dr. Dietmar Georg

Division of Medical Radiation Physics

Department of Radiotherapy

Medical University of Vienna

Währinger Gürtel 18-20, A-1090 Vienna

## Acknowledgement

First of all I want to thank Dr. Georg for his support and fast replies of my questions and his constructive and detailed feedback. Special thank also to Irina Fotina for all the time she spent with me, answering all my questions about basics as well as details. Furthermore she gave me plenty of tips how to write my master's thesis.
I also want to thank my family for the strong support. Without their appreciation the way my education took place would not be possible. Furthermore I want to thank my girlfriend for her strong belief in me and my skills, her support and the motivating talks with her.
I also want to thank my colleges and friends at my swim group, who helped me a lot with stimulating discussions and tips.

Thank you very much!

# Contents

# 1 Abstract

Conventional radiation treatment concepts are using one treatment plan for the whole course of irradiation. This plan is achieved by creating a "snapshot" of the patient using CT images. To overcome possible anatomic variations safety margins are added around the gross tumor volume. Advances in radiation therapy led to image-guided radiation therapy (IGRT), which utilizes actual images of the patient right before treatment. Therefore anatomic movements can be compensated effectively and safety margins can be minimized. However, anatomic deformations can not be compensated. Further progress in imaging techniques enabled the representation of day-to-day variations in the anatomy of patients and introduced the concept of adaptive image guided radiotherapy. There plans are recalculated according to daily anatomic changes inside the patient, including deformations. Recently the idea of using cone-beam CT (CBCT) images not only for for verification of the patient position and monitoring of the anatomic changes, but also for the treatment planning became popular. The ultimate goal would be the use of CBCT images for adaptive planning and dose calculation to provide the possibility of real time planning right before treatment takes place. This would provide a tool to adapt all types of anatomical changes inside the body, including movement and deformation. Therefore safety margins around tumor tissue could be dramatically reduced or even removed without harming healthy tissue at all.
The aim of this thesis is to investigate the applicability of different approaches for dose calculation based on CBCT images. Therefore four different adjustment techniques are used: two conversion curve-based and two non-conversion curve-based techniques. Dose calculation results are compared to results of planning CT and patient group specific conversion curve- based technique, described previously in literature. In detail, dose distributions are calculated by a commercial Monte Carlo algorithm. The outcome of dose calculations is analyzed by comparison of dose-volume histograms (DVH) and gamma evaluation. The outcome will be discussed concerning the accuracy of the methods compared to CT-based planning and applicability in clinical practice.
Differences below 3% for PTVs and OARs compared to planning CT demonstrate reasonable accuracy of the dose calculation for CBCT-based methods together with the required sensitivity to detect anatomic changes in the IGART process. Especially a simple approach using only 3 densities, showed high accuracy combined with a high clinical applicability, due to the small workload required.

# 2 Thesis Outline

The essential idea of this work is to compare different methods for CBCT based online adaptive radiotherapy. However, CBCT scans do not provide correct Hounsfield Units (HU) and cannot be used directly for dose calculation. This conversion is one of the most crucial parts to provide the possibility of real time, online replanning. Furthermore, this work will compare different approaches of CBCT-based ART, without the usage of HU-ED conversion curves (CC), to obtain the electronic density. The essential idea is to avoid the need of HU-ED conversion curves because of the high amount of time needed to obtain either patient specific or group specific conversion curves. Furthermore we try to find a method which is highly insensitive to impaired image quality of CBCT, caused by imaging artifacts and scattering. Therefore we aimed to develop two additional methods which use density informations of the CT images.
CT- and CBCT- plans for 30 patients (10 prostate-, 10 lung- and 10 head and neck-carcinoma) are created and evaluated. The different CBCT approaches are compared to both, CT plans and population-based conversion curves by $\gamma$- and dose-volume-histogram (DVH) evaluation. Furthermore, dose distributions for PTV, organs at risk and normal tissue are compared to planning CT based distributions. Additionally dosimetric errors are discussed as well as the clinical applicability of all approaches.
In the third chapter of this work an introduction to advanced radiology is presented. It includes basic principles of structure definition in radiation oncology, a short overview about the history of radiation therapy as well as basics of intensity modulated-, stereotactic- and image guided radiation therapy. It concludes with basics of adaptive radiotherapy. In the fourth chapter materials and methods of this work are presented. It consists of cone-beam CT fundamentals and explains the workflow for planning and CBCT-based recalculation. Furthermore the different comparison strategies of this work are presented. The final results and analysis of the data are presented in the fifth chapter. Finally a summary of the results of this work and an outlook are shown in chapter six. It is divided into three parts. In the first part all different HU-adjustment techniques are compared to the population- based conversion curve method by DVH evaluation. In the second party $\gamma$- evaluation is performed and in the third part the two most promising HU- adjustment techniques are compared to CT data.

# 3 Introduction to Advanced Radiation Oncology

In this section basic principles of advanced radiation therapy, including various treatment approaches, are presented. First structure definition for radiation therapy according to ICRU is explained. Afterwards a short summary of the history of radiation therapy and especially intensity modulated radiation therapy (IMRT) and stereotactic body radiation therapy (SBRT) are explained. Due to the usage of IMRT and SBRT in this work, both techniques will be explained in more detail. At the end of this section further developments in radiation therapy, including adaptive treatment planning, is explained.

## 3.1 Structure Definition for Radiotherapy

The definition of the target volume and of critical structures is a crucial and complex process in three dimensional conformal radiation therapy [27]. In a planning system, based on anatomical imaging like computed topography (CT) or magnetic resonance imaging (MRI), the radiation oncologist is required to outline the target volume to be irradiated, and the organs of risk to be spared, because of possible side effects [27]. To provide a standardized nomenclature for three-dimensional conformal treatment planning to the radiation oncology team a consistent language and guidelines for image based target volume delineation have been published in ICRU [1] report 50 (ICRU 50 1993), the ICRU report 62 (ICRU 62 1999) and the ICRU report 83 (ICRU 83 2010) defining the following terms [27]:

- gross tumour volume (GTV)
- clinical target volume (CTV)
- internal target volume (ITV)
- planning target volume (PTV)
- treated volume
- irradiated volume

In the book "new technologies in radiology" [27] the various volumes are explained in a very compact and clear way, wherefore direct citations of the book are presented in the following sections.

### 3.1.1 Gross Target Volume

"The gross tumour volume (GTV) is the macroscopic (gross) extent of the tumour as determined by radiological and clinical investigations (palpation, inspection). The GTV-primary (GTV-P) defines the area of the primary tumour and GTV-nodal (GTV-N) the macroscopically involved lymph nodes. The GTV can represent the total volume of the primary tumour, the macroscopic residual tumour tissue after partial tumour resection or the region of recurrence after either surgical, radiation or chemotherapeutic treatment. The delineation of the GTV is usually based on data obtained from CT and MRI." [27]

[1] International Commission on Radiation Units and Measurement, http://www.icru.org/

### 3.1.2 Clinical Target Volume

"The GTV, together with the surrounding microscopic tumour infiltration, constitutes the primary clinical target volume CTV (CTV-P). It is important to mention that the definition of the CTV-P also includes the tumour bed, which has to be irradiated after a complete macroscopic tumour resection, in both R0 (complete microscopic resection) and R1 (microscopic residual tumour on the margin of the tumour bed) situation. As the margins between CTV and GTV are not homogenous, they have to be adjusted to the probable microscopic tumour spread. The CTV-nodal (CTV-N) defines the assumed microscopic lymphatic tumour spread, which has also to be included in the radiation treatment planning." [27]

### 3.1.3 Internal Target Volume

"The internal target volume (ITV) is a term introduced by the ICRU report 62. The ITV encompasses the GTV/CTV plus internal margins to the GTV/CTV, caused by possible physiological movements of organs and tumour, due to respiration, pulsation, filling of the rectum, or variations of tumour size and shape, etc. It is defined in relation to internal reference points, most often rigid bone structures, in an internal patient coordinate system." [27]

### 3.1.4 Planning Target Volume

"The planning target volume (PTV) incorporates the GTV/CTV plus margins due to uncertainties of patient setup and beam adjustment; therefore, these margins consider the inaccuracy in the geometrical location of the GTV/CTV in the irradiated space, due to variations in patient positioning during radiotherapy and organ motility. The PTV can be compared with an envelope and has to be treated with the same irradiation dose as the GTV/CTV. Movements of the GTV/CTV within this envelope should not change the delivered radiation dose to the GTV and CTV. The setup margins are not necessarily uniform." [27]

### 3.1.5 Treated Volume

"The treated volume is the volume of tumour and surrounding normal tissue included in an isodose surface representing the irradiation dose proposed for the treatment. As a rule this corresponds to the 95% isodose. Ideally, the treated volume should correspond to the PTV; however, in many cases the treated volume exceeds the PTV." [27]

### 3.1.6 Irradiated Volume

"The irradiated volume is a volume included in an isodose surface with a possible biological impact on the normal tissue encompassed in this volume; therefore, the irradiated volume depends on the selected isodose curve and the normal tissue surrounding the tumour. The choice of an isodose surface depends on the end point defined for possible side effects in normal tissue." [27]

In *figure* 1 the different concepts used in target volume definition according to ICRU 50 and ICRU 62 is presented.

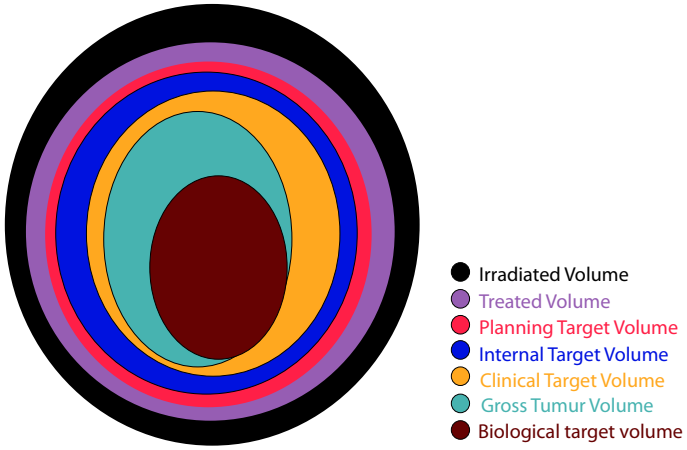


Figure 1: Concepts used in target volume definition for radiation treatment [27]

### 3.1.7 Organs at Risk

Another absolutely important term is "organs at risk" (OAR) or "critical structures", which are defined in the ICRU report 50 as anatomical structures with important functional properties located in the vicinity of the target volume [27]. Since irradiation can cause pathological changes in normal tissue, with irreversible functional consequences, they have to be considered in the treatment planning by outlining them in the planning process, defining tolerance doses of the organs at risk in the treatment strategy and quantifying the applied dose to these areas [27]. OAR risk assessment can either be done by visualizing the isodose distribution or by means of dose-volume histograms (DVH) [27]. DVHs are a commonly used tool for dose evaluation and show applied amount of dose for a relative size of the irradiated volume (0-100%). In *figure* 2 an example for DVH is presented.

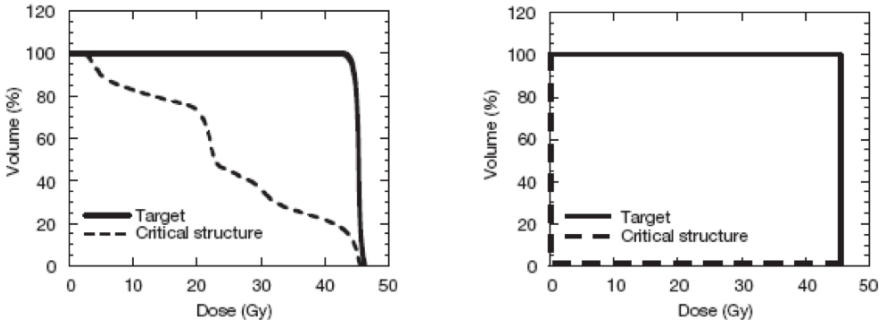


Figure 2: Example of a cumulative DVH for a case target-OAR together with the ideal DVH [24]

## 3.2 History of Radiation Therapy

In recent years the efficiency of radiation therapy has increased dramatically due to the high amount of research performed in this field. Different approaches have been developed to ensure for every type and location of cancer a constant dose in the tumor to damage all cancer cells effectively and to spare the surrounding healthy tissue. The early approaches of radiation therapy used planar radiographs to locate the tumor and rectangular fields to encompass the presumed tumor location. The radiation dose for healthy tissue located inside the field was the same as for the tumor [20]. The additional usage of various absorber blocks in the radiation field led to a major enhancement in the ability to conform the beam field according to the shape of the tumor. This method called conformal radiotherapy (CRT) was later on facilitated massively because of the advent of multileaf collimators (MLC), as time efforts and workload were drastically reduced [6]. With the introduction of medical computer tomography three-dimensional conformal radiation therapy (3DCRT) was developed which replaces conventional methods for tumor location like bony landmarks and air-tissue edges by target volume defined in a three-dimensional images of the patient [20]. MLCs allow the rapid, controllable and comfortable adjustment of field aperture by using a high number of small, movable absorber blocks which are moved by a computer automatically and is thus ideally suited for dynamic radiation beam modulation [20]. This was the requirement for intesity modulated radiation therapy (see chapter 3.3). In *figure* 3 an integrated MLC with a leaf width of 1 cm at the isocenter is presented.

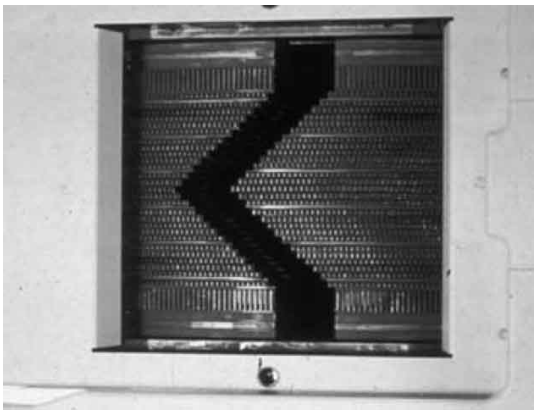

Figure 3: Example for an integrated MLC with a leaf width of 1 cm at the isocenter [27]

## 3.3 Intensity Modulated Radiation Therapy

The term intensity modulated radiation therapy (IMRT) was first introduced in the 1990s and it refers to a further development of 3DCRT. In contrast to 3DCRT which uses homogeneous incident fluences, IMRT provides the possibility to vary fluences throughout the radiation portal, with selection of the fluence intensities typically made using sophisticated algorithms [13] . Therefore the fluence of a beam is modulated not to be just "off" or "on" (ignoring

leakage)[2]. In *figure* 4 the working flow of a typical IMRT treatment, including 3D image acquisition, identifying and contouring anatomical targets and structures to avoid, defining the treatment goals and planning, is shown.

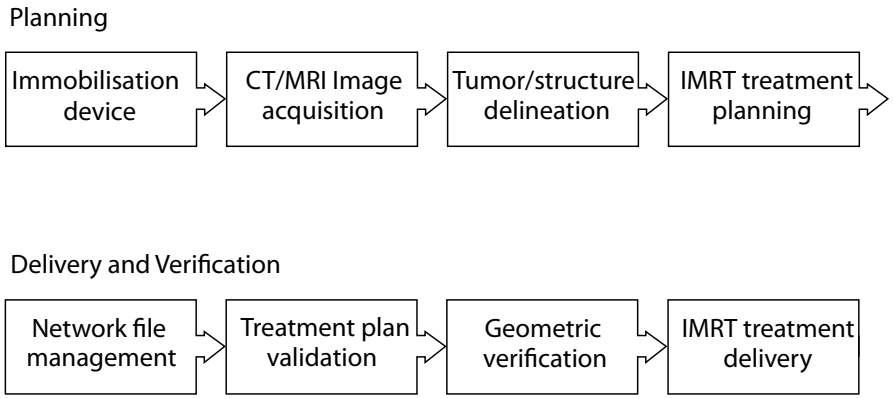


Figure 4: Principle workflow of an IMRT treatment [13]

According to Mundt et al.[20] the principle of IMRT can be summarized by the following statement: "Physically, a common feature of these IMRT techniques is that they all attempt to enhance control over the three-dimensional dose distribution through the superposition of a large number of independent segmented fields from either a number of fixed directions or from directions distributed on one or multiple arcs. Intensity modulation adds a new degree of freedom to RT planning and provides a more effective means to produce tightly conformal dose distributions in complex treatment situations.". In *figure* 5 a general comparison between CRT (top line) and IMRT (bottom line) is presented.
Due to the non-uniform radiation beam intensities which are determined by using various computer-based optimization techniques, IMRT supplies the advantage of higher target coverage especially at irregular concave shaped tumors, which provides dose escalation leading to better treatment outcome [34]. At the same time, IMRT provides better sparing of surrounding healthy tissues from receiving high dose radiation resulting in a decrease in adverse events leading to better quality of life [34]. Besides all these advantages of IMRT there are some disadvantages too, like the delivery of complex plans with traditional IMRT techniques takes extra time, the dose distribution in the PTV is more inhomogeneous compared to conformal techniques and higher number of monitor units (MU) in comparison with conformal plans, which leads to an increased peripheral dose, which again raises the generally increased low dose region furthermore [36].

### 3.3.1 Delivery Techniques

Historically there are various different ways to apply IMRT to the patient: mostly in literature the distinction is made according to the way the three dimensional dose distribution is achieved by superposition of segmental fields. This could be done either by a number of fixed directions ("Fixed- gantry IMRT") or

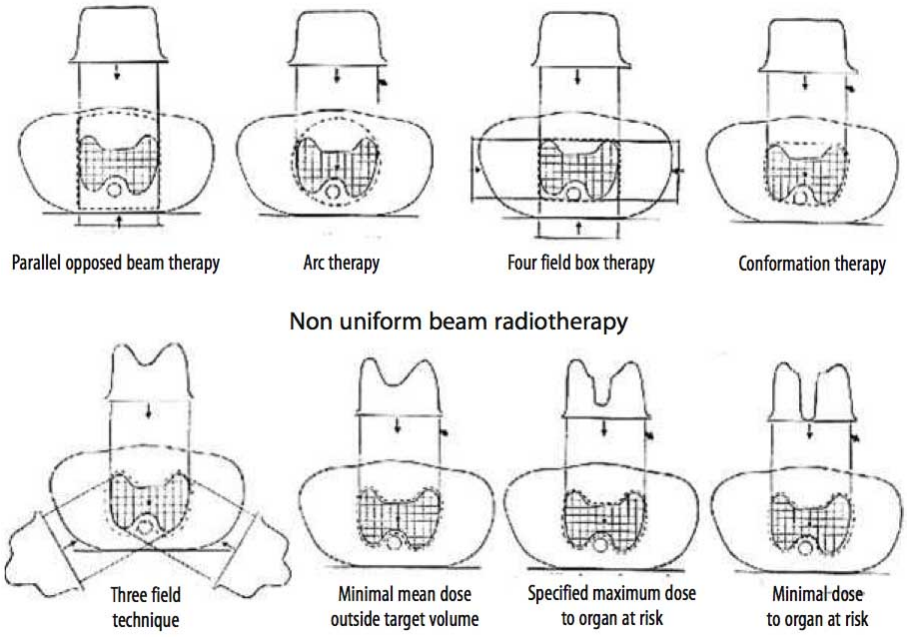


Figure 5: Conventional and intensity modulated radiation therapy (IMRT) dose distribution to a complex target volume (hatched) and critical structure geometry. The upper four figures indicate the dose distribution using conventional planning and delivery. The lower four figures indicate fixed-beam and arc-based IMRT with different optimization criteria [13]

a number of directions distributed on one or several arcs ("Arc-based IMRT"). Another very common method to distinguish various approaches is to by the way the beam intensity is modulated: dynamic or static [2].

**Fixed-Gantry Delivery** At fixed-gantry delivering technique a number of fixed beam directions is superimposed to achieve the desired dose in the tumor, utilizing the replacement of lead blocks, intentionally used to shield normal tissue during the treatment, by MLCs in modern linear accelerators [13]. Based on the MLC computer-control system, two main dose delivery methods are distinguished: on the one hand the so called "segmental MLC delivery" and on the other hand "dynamic MLC delivery" [6] [27] [35].
The first strategy is also called "step-and-shoot" (or "stop-and-shoot") technique of IMRT dose delivery and is a straightforward extension of the conventional multiple-field irradiation technique [6] [27]. It superimposes the dose delivered by a number of irregularly shaped and partially overlapping treatment fields, called subfields or segments, where for each segment a well-defined number of monitor units is delivered [27]. Then, in contrast to the dynamic mode, the beam is turned off while the leaves of the MLC move to the positions required by the next IMRT subfield. After the validation of the new leaf positions done by the verification and record system, the beam is turned on again and the dose is delivered for this segment. This process is repeated for all segments per incident beam angle and all beam directions [27]. In *figure* 6 the principle idea of the step-and-shot IMRT delivery is presented.

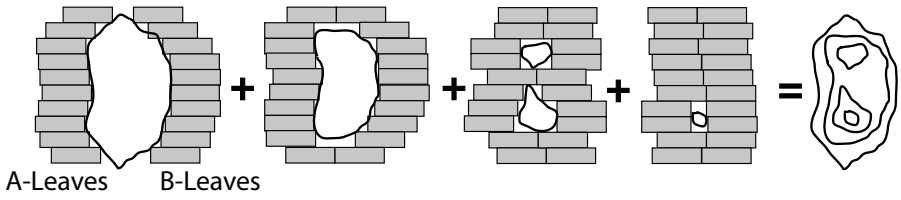


Figure 6: Basic principle of step-and-shoot IMRT delivery [27]. Between the different subfields the radiation is turned off until the MLC-elements are in the right position for the next subfield (segment).

The second strategy is also called "sliding window" and "DMLC" as it is called the dynamic approach [27]. Unlike the static delivery the intensity modulation in the dynamic delivery is achieved by an individual variation of the velocities of the moving leaves, which means that the treatment can be realized without interrupting the beam [27]. Each leaf pair of MLC moves continuously, unidirectionally, and with independent speed (while the beam is on) to modulate the beam, contrary to the static mode where the shaped MLC remains fixed while the beam is on, and modulation of the beam is achieved through a series of complex small-segmented subfields [30]. The working principle is illustrated in *figure* 7.
Comparing both strategies non of them is clearly superior to the other. According to Fotina [6] and Chui et al. [4] it strongly depends on the disease treated and the resulting priorities in treatment: The beam-on-time (Monitor Units,

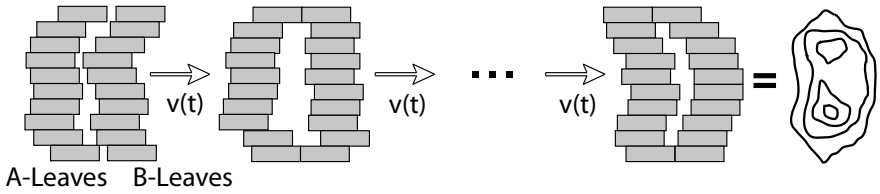


Figure 7: Basic principle of dynamic IMRT delivery [27]. During the whole treatment the radiation beam is turned on

MU) requirement for step-and-shot IMRT was approximately 20% less than at the dynamic approach, but the delivery time was about twice as long. But also other parameters like characteristics of the device like leaf speed, accuracy (for dMLC the leaf speed has to be controllable with a very high accuracy and that the calibration process for leaf speed and leaf position must be easily possible), quality assurance, target coverage, critical organ protection, beam-on-time and delivery time (generally shorter for dMLC) have to be considered [27].

**Arc-Based Delivery - "Tomotherapy"** Arc-based delivery systems were developed earlier than the fixed-gantry systems and are based on the essential idea to use a rotating gantry. Instead of a relatively small number (about 7) of fixed gantry angles, like sMLC, dynamic collimator changes produce a thin fan beam [3]. The fan beam is moved either helical or slice by slice while gantry rotation [3]. In the 1990s, arc-based IMRT started by the development of the "serial Tomotherapy" device, which was in fact the first commercial arc-based IMRT device available on the market [20]. Tomotherapy is a combination of the words "tomography" and "radiation therapy". Nowadays there are various different devices available for arc-based IMRT delivery.

**Serial Tomotherapy** The oldest arc-based commercial device was released 1996 by the PEACOCK System and was a "serial Tomotherapy", which means that the patient is "treated" slice-by-slice [20]. The architecture of a Tomotherapy (TT) device is quiet simple: mostly a 6 MV linear accelerator is mounted onto the gantry ring and directed towards the center of the gantry. Due to the usage of slip-ring technology, this device is capable of continuously rotating around a patient couch, enabling a smooth dose delivery [20]. In Fotina's work a very good description of the working principle of a serial Tomotherapy can be found:
"In a serial approach employed by the Peacock system the table is fixed during the rotation of the gantry through 270 degrees with the radiation beam on. The fan presents a narrow rectangular slit aperture much wider transaxially than longitudinally. After each rotation the coach is moved in longitudinal direction for the delivery of the next fan beam. The beam is collimated to a narrow slit and beamlets are turned on and off by driving the mini-MLC leaves out and in the beam path, respectively, as the gantry rotates around the patient. Each slice covers 2-4 cm and 20 cm in diameter. An advantage of this modality is that the MIMiC collimator can be retrofitted to an existing linear accelerator"

[6]. In *figure* 8 a picture of a binary MLC is presented.

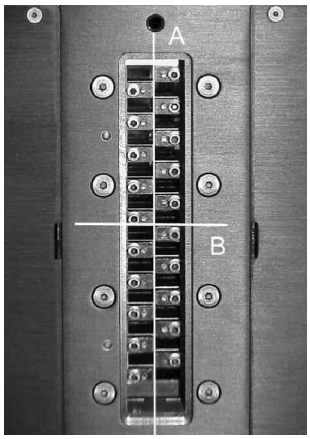


Figure 8: Binary collimator consists of two banks with 20 collimators each. The two sets (banks) of leaves (or vanes) can be seen with some open and some shut [20]

**Spiral Tomotherapy** The concept of "spiral tomotherapy" or "helical tomotherapy" was announced in 1993 [2]. For ten years the development and research departments worked on a prototype, which led to a device quite similar to the serial approach concerning radiation collimation (single slit of radiation with long axis transaxial to the patient) [2]. The major differences concern both, the number of elements in the binary MLC and the way the patient is moved during gantry rotation. Mostly the number of elements per line is increased from about 20 to 32 or 64 elements. The radiation is not delivered slice by slice but by continuous patient table feed, resulting in an CT-like slit beam executing a helical spiral trajectory [2] [6]. An added feature of the Tomotherapy system is an imaging system which allows the acquisition of megavoltage CT patient images [6]. Commercial systems use a detector on the opposite side of the radiation source. Due to image quality reasons the energy of the radiation source gets reduced to 1MeV during image acquisition.

In *figure* 9 a comparison between both Tomotherapy devices is presented.

**Intensity Modulated Arc Therapy** After years of development C. X. Yu [38] introduced a new technique called "Intensity modulated arc therapy" (IMAT) in 1995, which was a logical development of the multiple static field technique. Like tomotherapy, IMAT delivers photon radiation treatment in an arc manner, but instead of using rotating fan beams, IMAT uses rotational cone beams of varying shapes and varying dose weightings to achieve intensity modulation [39]. IMAT rotates the gantry a number of times, corresponding to the number of subfield components, delivering each component from each gantry angle at each rotation [6]. A major advance in IMAT was realized when K. Otto [22] implemented his volumetric modulated arc therapy (VMAT) al-

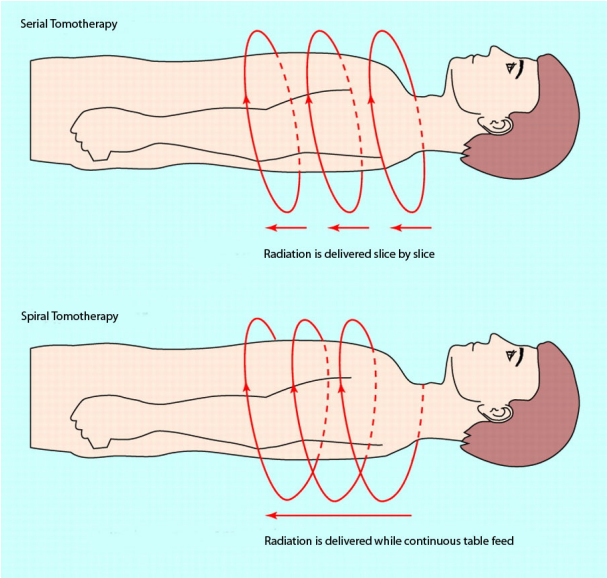


Figure 9: Comparison of the essential principles of serial- and spiral Tomotherapy. The original picture was found at http://www.bmj.com/content/324/7345/1077/F1.large.jpg. The text was modified

gorithm, which uses a progressive sampling algorithm to gradually improve the arc resolution by obviating this restriction and allowing large leaf movements early in the optimization and more restricted leaf motion in the later stages [21]. In general, the VMAT technique is similar to Tomotherapy in that a full 360°of beam directions are available for optimization. However, a fundamental difference is that the entire dose volume is delivered in a single source rotation [22]. There are also other commercial names for IMAT like "RapidArc" [2], which has the unique feature to use just one gantry rotation, and "VMAT" [3] where instead of Otto's algorithm a proprietary algorithm is implemented [21]. As compared with Tomotherapy, IMAT has some of the following advantages [39]

- IMAT does not need to move the patient during treatment and avoids abutment issues as seen with serial tomotherapy
- IMAT retains the ability of using non-coplanar beams and arcs, which has great value for brain and head and neck tumors
- IMAT uses a conventional linac, thus complex rotational IMRT treatments and simple palliative treatments can be delivered with the same treatment unit.

## 3.4 Stereotactic Radiotherapy

The word "stereotaxy" is Greek and consists of the two words "stereo" and "taxis", which means "orientation in space" [27]. Although the clinical appli-

[2]Varian Medical Systems, Palo Alto, CA, USA
[3]Elekta AB, Stockholm, Sweden

cation of stereotaxy in radiation oncology is quite new and used for only about 15 years, the idea itself has strongly been used in the past 50 years for other purposes like stereotactically guided needles and radiotherapy in neurosurgery.

Sometimes there is a confusion concerning the terms "stereotaxy", "radiosurgery" and "stereotactic fractioned radiotherepy" (SFR) because a general and world-wide consistent nomenclature is missing. Mostly the terms are used according to the number of fractions used for treatment: if there is only a single fraction stereotactic radiosurgery (SRS), if there are multiple fractions stereotactic (fractionated) radiotherapy (SRT) is used [27]. In *figure* 10 a widely spread classification is presented. The abbreviation "Tx" means treatment. Nonetheless, in this work the term stereotactic radiotherapy is used as a general term which contains both methods, single and multiple fractioned treatments.

Figure 10: Possible classification of stereotaxy according to the number of fractions applied and type of fixation [13]

| **Stereotactic Radiosurgery (SRS)** | **Stereotactic Radiotherapy (SRT)** |
|---|---|
| *Invasive fixation (stereotactic frame)* | *Non-invasive fixation (images used)* |
| Stereotactic frame placement (30min) | Imaging and Tx planning (Day 1: 60min and 360min resprectively) |
| Pre-Tx imaging (30-90 min) | Pre-Tx imaging (Days 4,7,9: 45min per Fx) |
| Tx Planning (15-120min) | Tx isocenter adjustment (5-15min per Fx) |
| Patient treatment (15-150 min, 1Fx) | Patient treatment (30-45min per Fx) |

The essential idea of stereotaxy is to define a point in the patient's body by using an external three-dimensional coordinate system which is rigidly attached to the patient. Stereotactic radiotherapy uses this technique to position a target reference point, defined in the tumor, in the isocenter of the radiation machine very accurate [27]. "In general, the stereotactic coordinates are a cartesian three-dimensional coordinates system attached to the stereotactic frame in a rigid relationship. The origin of the stereotactic coordinates system is generally in the center of the volume defined by the stereotactic frame: the x and y axes correspond to the lateral and frontal side of the frame and the z axis to the cranio-caudal direction." (see *figure* 11) [27].
An absolutely necessary requirement for stereotaxy is the patient immobilization and repositioning with either an invasive frame, a non-invasive frame, or a frameless system to direct precise radiation beam targeting to achieve positioning accuracies as small as 1mm [13]. In practice the stereotactic localizers (for example CT-compatible fiducial markers in each plane) are mounted on the frame which is rigidly fixed to the patient and subsequently imaged with the patient. This procedure allows a transfer of the image coordinates into the stereotactic coordinates system [27]. Due to the elevated spatial accuracy it is possible to reduce or even to remove the safety margins around the gross tumor volume (GTV) at planning the planning target volume (PTV) resulting in higher sparing of normal tissue [27].

Stereotactic treatments can be performed either on conventional linear accel-

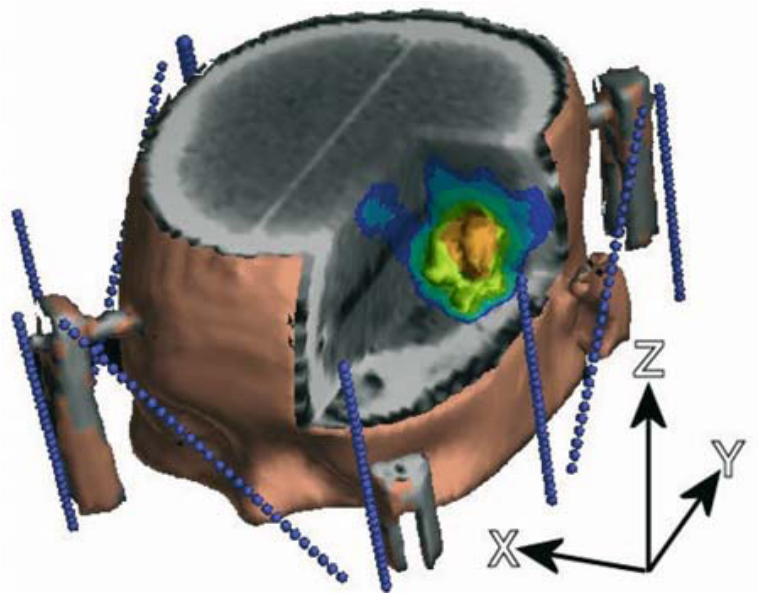


Figure 11: Stereotactic frame, localizers and stereotactic coordinates [27]

erators with MLCs or conical collimators, or on especially designed devices like the Gamma Knife or Cyberknife.

The Gamma Knife, the first dedicated device for stereotactic SRT delivery consists of 201 $^{60}$Co sources which were arranged on the surface of a hemispherical shell, each aiming at an isocenter in a uniform distance of 400 mm. They are collimated by one primary and 201 secondary collimators which are placed on a helmet the patient wears during treatment [27]. The helmet produces a spherical dose distribution at the isocenter, where the area of interest lies. The diameter of the sphere depends on device properties and can be between 4mm and 18mm [27]. For complex, irregular structures conformal dose distributions are created by a sequence of treatments with different isocenters [27]. This can by realized by using different diameter helmets [27]. In the 1980s the $^{60}$Co sources were more and more replaced by the LINAC. Kurup [12] describes the improvements of LINAC based stereotaxy as follows:
"The 'linear accelerator'-based radiosurgery was pioneered in the mid-1980s. These systems differ from the original Gamma Knife system in many ways. 6-MV x-rays produced from linear accelerator are used in these systems, instead of gamma rays from Co-60 sources. All these systems were used in conjunction with a stereotactic frame fixed onto the skull of the patient. Three-dimensional coordinates of the tumor were precisely determined by the stereotactic frame, and the radiation was delivered accurately to the target volume. Small circular collimators fitted at the end of the treatment head as tertiary collimators were used for narrowing the beam of x-rays from a conventional linear accelerator. All these systems require a stereotactic frame to be fixed onto the patient's head, right from imaging to treatment, and hence are termed as invasive or minimally invasive procedures. These methods of conformal dose delivery to the target

reduce radiation dose to the surrounding normal tissues substantially." [12]
The basic workflow is quite similar to the procedure in other radiation treatment techniques: After images for treatment planning (according to the technology either with or without a stereotactic frame), the data is processed in the treatment planning system (TPS). The size and shape of the beams are selected by hand and the required irradiation time is calculated by the TPS. An example for rotational stereotactic technique using six radiation arcs and conical collimators is presented in *figure* 12.

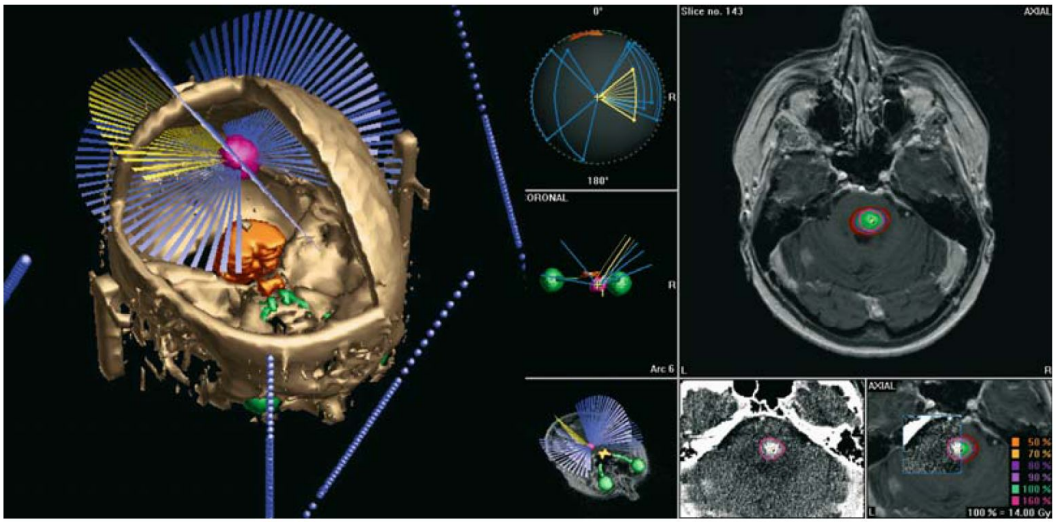


Figure 12: "The images left show the rotational stereotactic technique using six radiation arcs and conical collimators. The images right present the dose distribution for the radiosurgery treatment of a brain stem metastases on MRI (upper) and the CT/MRI image fusion (lower)" [27]

A few years later stereotaxy experienced other major improvements due to the development of non-invasive, replaceable head-fixation systems, which allowed the implementation of the dose fractionation and the micro-multileaf collimator which permitted the adoption of the irradiated area to irregular-shaped target volumes as well as the rapid dose fall-off outside the target volume [27] [13].

In the 1990s a new, completely different stereotactic device, developed by Dr. John Adler, a neurosurgeon in Stanford, USA, called "Cyberknife" came into practice. In contrast to conventional stereotactic devices Cyberknife consists of a lightweight linear accelerator fitted onto an industrial robot with 6 degrees of freedom of movement, while conventional LINACs have only rotational movement in one plane, which makes treatment highly precise [12]. In *figure* 13 a modern Cyberknife device is shown.
Other major advantages of Cyberknife are non-isocentric treatments, where beams can be directed from any desired angle as well as the omitting of a rigid frame to be fixed onto the skull of the patient for stereotactic setup and verification [12]. Unlike other LINAC-based systems, which have accuracy in millimeters, the Cyberknife provides sub-millimeter accuracy in tracking tumor position. This is guaranteed due to orthogonal x-ray images which are taken


Figure 13: Modern Cyberknife system of 2010 [10]

before each beam and verified during or after the treatment - if sub-millimeter accuracy is not achieved, it gives a warning and stops treatment [12]. However, there are also disadvantages of the Cyberknife system including long planning times for difficult cases and long treatment times for anatomically large tumors [17]. In *figure* 14 an illustration of the CyberKnife System treatment beam geometry is shown.
Initially designed for intracranial treatment, further development of Cyberknife enabled also extracranial treatment like liver- and lung-tumors, providing an unique whole-body stereotactic radiotherapy system.

## 3.5 Treatment Planning Systems

Treatment planning prior to the 1970s was carried out through the manual manipulation of standard isodose charts on the patient body contours. They were generated by direct tracing or lead wire representation, and relied heavily on the judicious choice of beam weight and beam shape [24]. The development of CT, combined with the readily accessible computing power from the 1970s on, led to the growth of CT based computerized treatment planning systems, providing the ability to view dose distributions directly superimposed upon a patient's axial anatomy [24] [6]. This is also called "forward based treatment planning" and was in fact a trial and error approach by experienced professionals [24].

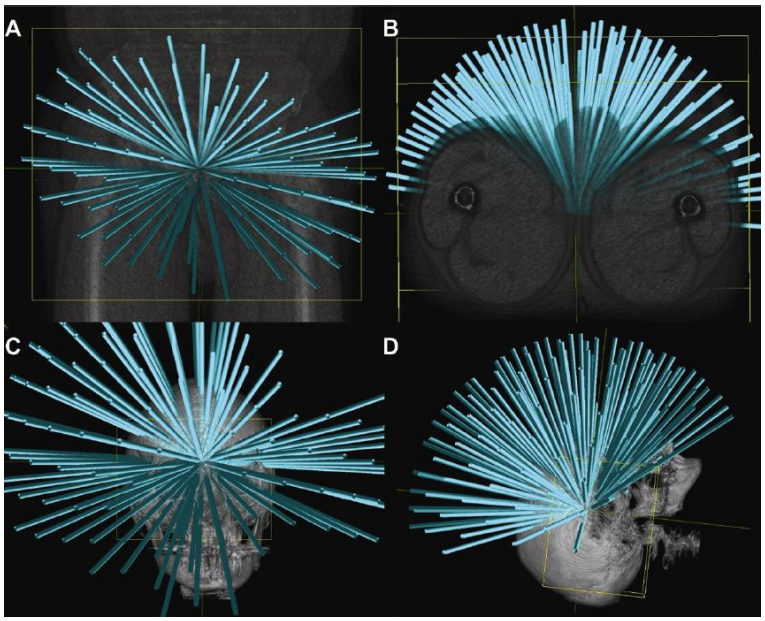


Figure 14: Illustration of the CyberKnife System treatment beam geometry [10]

For IMRT treatments mainly "inverse treatment planning" (ITP) is performed by treatment planning systems (TPS). ITP describes a computer optimization method of determining the nonuniform beam-fluence profiles that lead as close as possible to the desired dose distribution. Inverse problems in general therefore can be described as problems in which the output or consequences are known but not the cause [6]. After obtaining the images of the patient, which can be either single- or multimodal (according to the recognizability of tumor), eventually image fusion is performed. This is followed by a reconstruction of three dimensional images / volumes by the TPS. In the next step the clinician defines the different structures by indicating both, the OAR as well as target volumes and normal tissue slice by slice. Afterwards the TPS determines the desired shape of the dose distribution, intended to maximize dose in the target volume and minimize dose to surrounding tissues. This is achieved through specifying the arrangement, size, shape, and weight of the beams utilized. The best solution is found by calculating a defined mathematical objective function consistent with the previously defined constraints [9]. The latter consists of both, statements that should always be hold ("constraints"), like "no more than 45Gy should be delivered to an OAR", and functions that should be as small or large as possible ("objective functions"), like "the average prescription doses and the computer-predicted doses should be as small as possible" [9]. The objective function includes terms for normal tissues as well as target volume and is a weighted sum, which represent the relative importance of these terms [9]. Modern TPS use "dose-volume-constraints", which are a different input method for constraints: the planner determines that not more then $x$ percent of an organ (volume) receives $y$ dose [9]. Meyer et al. [9] describes the steps afterwards as follows:
"After the objective function is specified, the incident beams are typically ide-

alized by mapping them into small discrete elements, called beamlets. Each beam is mathematically modeled, comprised of a sum of these beamlets. Typically, thousands of such beamlets are used in the first part of the optimization process. The aim is for the computer to determine the best or "optimal" beamlet weights. In the computer, beamlets are represented as close contributions to different voxels for a given level of beam monitor units (for example, dose for 1 monitor unit). The overall dose to a volume, for instance a target volume, will be the weighted contributions of all of the beamlets from all beams. Most commercial systems take the approach wherein beamlet fluences are first optimized and afterwards MLC settings are derived as a deliverable sequence. This is the most common approach, although some companies are considering an approach that starts with apertures, and directly modifies or optimizes the aperture shapes. Once all the terms are put together into an objective function, and the beamlet matrices are computed,the computer is asked to iterate the beamlet weights until objective function progress between iterations falls to a specified low level. In actual practice, it is always a problem to tell when you should cut off the optimization iterations, and it is often not very clear at all when you are done."[9]
In clinical practice the "best plan" is achieved if the plan cannot be improved without major efforts.
"After the beam fluence maps have been derived, they must be broken up (decomposed) into deliverable segments for each beam that the MLC can deliver in a stepwise fashion. For some systems, the beam can be on when the segment is delivered, even when the MLC leaves are moving (dynamic delivery). Otherwise, the beam is off when the MLC leaves are moving between segments (static or step-and-shoot delivery). The many resulting segments together comprise the full delivery of the fluence map. An attempt to reconstruct that fluence map (as well as possible) is made by the superposition of these segments, but there is always some discretization error (usually but not necessarily small)." [9]

An additional feature of modern TPS include, beside inverse treatment planning, treatment simulation and verification also possibilities for dose exports, like to create an output file which consists of raw dose values for each voxel of a slice. Furthermore, printable summaries of the treatment, comparison of different treatment approaches by DVH- and slice by slice isodose-comparison as well as other features are common.

## 3.6 Image Guided Radiation Therapy

Radiation therapy has experienced a remarkable evolution from its classical 2D approach to 3D techniques that design the treatment based on image-derived 3D models, providing tools to assess and consequently potentially adapt the treatment to the response and the movement of the patient [11]. Due to the introduction of three dimensional anatomical and functional imaging techniques, like CT and MRI, the way target volumes are defined changed dramatically from derived 2D anatomic parameters to customized targets based on multimodality imaging (MMI) [11]. The subsequent clinical implementation of refined conformal delivery techniques such as IMRT and stereotactic body radiotherapy (SBRT) offer the ability of sharp dose gradients resulting in increasing precision and accuracy in radiation delivery [11] [1]. In clinical practice this will lead

to reduced toxicity with the potential for dose escalation and improved tumor control [11]. However, due to the high conformity of the dose to the tumor volume and the rapid dose fall off outside the tumor volume, the accuracy of daily treatment delivery is crucial, otherwise a geographical miss of the tumors or overdose to the OARs could be possible [11] [1]. It is, therefore, essential that the patient position is accurately reproducible, unaffected by daily inter-fraction motion and intra-fraction motion [33] [11].
IGRT aims at reducing geometrical uncertainty introduced by the patient's anatomical movement (see chapter 3.1 ), resulting in a smaller CTV-PTV margin, which decreases again the consequent collateral damage to normal tissues [28] [11]. IGRT is implemented for therapies where daily imaging is common (e.g. prostate cancer) and holds that images will be taken daily to evaluate the patient geometry at treatment [23]. According to the information obtained by the latest images the patient position is altered [11].
There are two types of set-up uncertainties, systematic and random. The systematic error can be caused by the fact that a 3D image acquired during CT simulation is just a snapshot, and the target position determined at that instant of time may differ from the average target position [15]. Furthermore, a systematic error may also be produced if an error is reproduced many times, like wrong positioning of the patient for all examinations. In contrast to that the random error is the day-to-day deviation from the average target position [15]. Of the two, systematic uncertainty is more important, because if uncorrected it would be propagated throughout the treatment course, and lead to harming effect on local control [15].
Due to the adaption of the patient position according to images obtained right before treatment, IGRT has the potential to increase accuracy and therefore also the potential success of radiation therapy treatments. Technically sparing of healthy tissue and irradiation of tumor tissue are kept on constant level, although the position may change. Basically two different types of IGRT are used in clinical practice, which are classified according to the usage of the images obtained prior treatment. On the one hand they can be used after the treatment delivery to be evaluated retrospectively, which is also called "offline approach", or they are used prospectively, which is called "online approach" [11]. In contrast to online IGRT, where random and systematic errors can be eliminated, offline verification just aims to eliminate any systematic error between planning and treatment. Although it is both, technically easy to achieve and more cost effective, Ling et al. [15] describe the clinical acceptance and usage of offline evaluation as follows:
"Offline adaptive correction protocols, if judged clinically beneficial to account for systematic error or tumor changes (e.g. shrinkage), can be easily realized using CT simulator during the treatment course, followed by a new treatment plan if warranted. This option, while technically available in most departments, is rarely used to make mid-course corrections to the treatment plan". The challenge with the online approach is to integrate the verification and correction process in the treatment chain smoothly to minimize the time the patient is on the treatment couch while the images are analyzed, a decision made and corrections performed [11].
Technically there are two major classifiers to categorize 3DCT-IGRT solutions, namely beam quality (whether they are based on megavoltage or kilovoltage beams) and beam collimation (whether they are cone-beam or fan-beam solu-

tions, where the former uses an open beam and large-area flat panel detector, whereas the latter applies a linear array of detectors in combination with a fan beam) [11]. Due to the possibilities four different configurations are possible:

- Kilovoltage fan-beam CT (kV CT)
- Kilovoltage cone-beam CT (kV CBCT)
- Megavoltage cone-beam CT (MV CBCT)
- Megavoltage fan-beam CT (MV CT)

### 3.6.1 Kilovoltage Fan-Beam CT

This was the first approach of IGRT with the essential idea to place a CT-scanner inside the treatment room, which is also called "CT on rails" [11]. The advantage over planar imaging for localization and verification is obviously the availability of 3D information and the visibility of soft tissue in the CT-scan [11]. There are two possibilities to acquire CT images for the patient set-up, either with the treatment table of the actual treatment LINAC, where the patient on the treatment couch must be moved between the scanner and the treatment unit, or with the CT-scanner moved to/from the patient [11].

### 3.6.2 Kilovoltage Cone-Beam CT

Here a gantry-mounted X-ray source produces the CT images for patient set-up, solving the problem of patient movement after imaging [11]. The imaging components, a conventional CT X-ray source and flat panel detectors, where the imaging axis is mostly chosen at a 90°angle with the treatment beam, are mounted to the linac gantry [11].

### 3.6.3 Megavoltage Cone-Beam CT

According to studies performed in the 1980s a major problem with these approaches was unaccurate table positioning using the treatment couch [11]. To overcome this problem, feasibility studies on 3D MV CBCT using an additional portal imaging detector were performed [11] [19]. In detail CCD scintillation detector camera-based EPIDs were mounted on the LINAC, with the image frame acquisition synchronized with the radiation pulses [11]. Pouliot et al. [25] have reported on the clinical feasibility of this approach. Advantages of megavoltage imaging include that the actual treatment beam is used for imaging and that no additional hardware is needed [11]. Furthermore, the imaging dose can relatively easy be incorporated into the dose calculation algorithm because a megavoltage beam is used for treatment as well. [11]. However, the drawbacks like lower soft tissue contrast have to be considered as well.

### 3.6.4 Megavoltage Fan-Beam CT

With the helical tomotherapy solution, a concept was introduced using the ring MV gantry for helical fan-beam MVCT imaging just prior to treating with the same gantry, which is now the most widely used solution for in-room MVCT imaging [11].

### 3.6.5 General Risk of IGRT

However, there is some evidence in literature that the technical precision provided by IGRT also induces a potential danger as to reducing margins to levels that are inadequate, for instance because they ignore inherent clinical uncertainty in target delineation [11]. Additional the whole essential idea of IGRT naturally leads to the question concerning the risk of imaging dose [23]. In detail, the issue of peripheral dose to create CBCT images, which is dependent on a number of factors relating to the quality desired in the images, has to be considered as well [23].

## 3.7 Adaptive Treatment Planning

The next huge step in development of IGRT is called image-guided adaptive radiotherapy (IGART) and uses adaptive treatment planning (ATP). Additional to IGRT, where 3D soft tissue target matching and repositioning is applied, in adaptive treatment planning also the treatment plan with respect to anatomical changes that occur during the radiotherapy treatment course is adapted [11]. Due to the essential idea of IGRT, it only corrects rigid errors due to changing the patient position by moving the table, while ART additionally provides the power of changing non-rigid errors, like deformations [29]. This is necessary due to the significant change of the location, shape and size of disease and normal anatomy due to daily positioning uncertainties and physiological factors during a course of treatment [29] [8]. In *figure* 15 a typical ART workflow diagram is presented.

In other words: ART is an approach to correct daily tumor and normal tissue variations, including both position variation deformation, through online or offline modification of original IMRT target volumes, IMRT organs-at-risk (OAR) and plans [14] [29]. In *figure* 16 typical changes in volume of prostate during treatment course is presented to motivate ART.

The overall success of clinical application of ART depends on three basic components: detection of changes, method of intervention and management of overall clinical goals [29]. The major goal in recent research is to fulfill these basic requirements. Additional a fast online replanning algorithm for adaptive radiation therapy programs has to be provided to enable clinical application [14]. The approaches of ART can be categorized into two groups according to the type of plan [14]:

- for fluence map-based IMRT plans, modifying MLC leaf positions directly based on changes in anatomical structure positions and shapes
- for direct aperture optimization- (DAO-) based plans, modifying the aperture shapes and weights using the projection of the target-organ deformation information

Although these methods feature fast adaptation, they are based on manipulating either 2D fluence maps or discrete 2D beam apertures in the attempt to approximate the 3D target-OAR geometry variation and regain the 3D dose

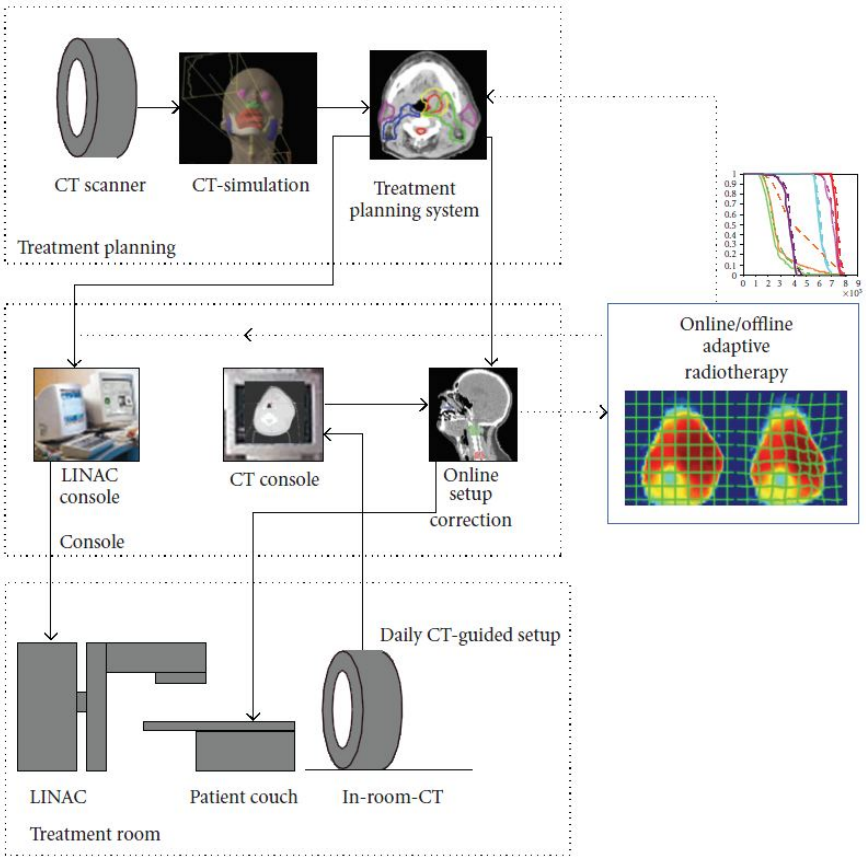


Figure 15: A workflow diagram for in-room CT or CBCT-guided adaptive radiotherapy. The first level of treatment modification is a simple couch shift to correct for daily setup errors (CT-guided IGRT). Nonrigid changes in tumor volumes and normal organs can then be corrected via an online or offline adaptive replanning process (dotted lines) [29]

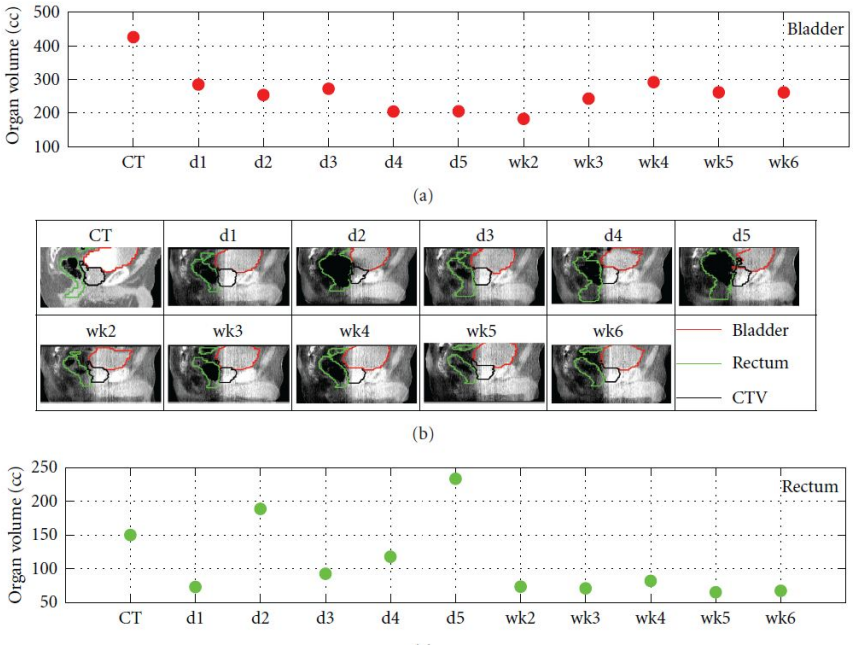


Figure 16: Daily structure variations of one patient due to bladder and rectum fillings. Eleven images are shown in this figure, namely one planning CT and 10 cone-beam CT (CBCT) images taken once per day for the first 5 days of treatment (d1-d5), and once per week thereafter (w2-w6). Colored contours: red-bladder, green-rectum, black-CTV. [14]

conformality of the original plan [14]. Another approach is to reoptimize the fluence map based on the initial IMRT plan (dose distribution) directly [14]. This approach uses deformation fields to deform the original dose distribution to adapt daily anatomic movements [14].

# 4 Materials and Methods

## 4.1 Cone-beam CT

### 4.1.1 Introduction

As already described in section 3.7, imaging right before treatment is necessary for IGART. In contrast to planning CT, CBCT imaging devices may be mounted on the LINAC. Therefore patient images can be obtained on the treatment couch in an already fixed position right before treatment. Although megavoltage CBCT imaging is possible, kilovoltage CBCT imaging is used in this work (see section 3.6).
The first prototype of a clinical cone beam computed tomography (CBCT) scanner was presented in 1982 and designed for angiographic applications. It took more than ten years until the first commercial CBCT scanners were available, strongly driven by the parallel advancements in flat panel detector (FPD) technology, improved computing power, and the relatively low power requirements of the x-ray tubes used in CBCT [18]. In recent years cone-beam computed tomography became standard in the radiation therapy process, due to its ability to acquire full three dimensional (3D) images of the patient on the treatment couch in treatment position [7]. Like conventional CT, a CBCT scanner consists of a kV x-ray source and an opposing detector, but instead of an detector array, a two dimensional detector matrix is used [7] [5]. As detector elements mostly digital FPDs, which enable the direct conversion of x-ray energy into a digital signal with high spatial resolution, are used [5]. Another striking difference between CT and CBCT is the beam geometry: in CBCT systems, the x-ray beam forms a conical geometry between the source and the detector, which is in contrast to conventional fan-beam geometry [18]. In *figure* 17 the different beam geometries of CT and CBCT are presented.

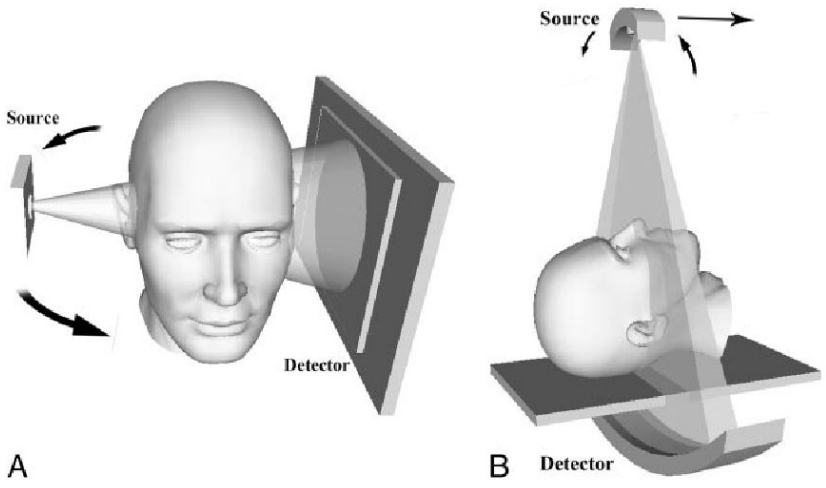


Figure 17: Depiction of CT acquisition geometries: on the left side a cone-beam geometry, on the right side a conventional fan-beam geometry as it is used in CT scanners.[18]

The principle design of CBCT allows to mount both, the source and the detector, on a retractable arm onto the linac gantry at 90°to the treatment head, which enables the acquisition of kV X-ray images for radiography, fluoroscopy and CBCT [7] [5]. To provide exact imaging of the patient in treatment position, the central axes of the kV imaging beam and the MV treatment beam should nominally cross at the isocenter [7]. To provide three dimensional information, a set of planar images by a cone shaped beam is acquired while the gantry of the linac rotates around the treatment couch [7]. A 3D volumetric image is then reconstructed from this series of planar projection images by the software of the imaging system with the use of a backprojection algorithm [7]. In *figure* 18 the idea behind backprojection as well as the working principle of CBCT is presented.

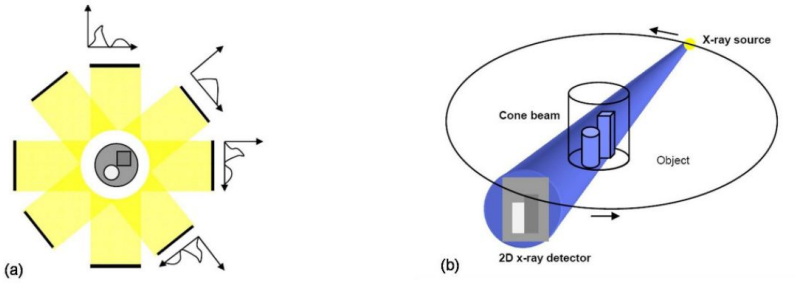


Figure 18: a) The principle of backprojection and b) build up of a CBCT system.[7]

Advantages provided by CBCT are faster reconstruction time, because just one rotation of the head is needed, therefore less blurring and less radiation dose in contrast to conventional CT, imaging in treatment position is possible as well as a reduced cost price [5]. Nonetheless there are also disadvantages like higher x-ray scattering, therefore a reduced SNR [4], smaller field of view (FOV) as well as different artifacts [5]. Hopfgartner [7] describes the most common artifacts of CBCT as the following:

**Ring artifacts** "Ring artifacts are concentrically arranged circles in a CBCT image. They fake alternately more and less attenuating material. Possible reasons of such image disturbance are detector malfunctions such as a defect of single detector elements." [7]

**Streak artifacts** "Streak artifacts appear as streaks or lines through the image. Most of them arise from the fact that the detector is susceptible to discontinuities of adjacent projection images from various sources. Possible causes of such discontinuities are aliasing effects due to the limited number of acquired sample images and beam hardening effects due to shadowing phenomena because of high atomic number materials." [7]

[4]Signal to noise ratio

**Cupping artifacts** "Cupping artifacts are deviations from an overall consistency of HUs across a homogeneous scan field. These make attenuation coefficients near the edges of scanned object to appear lower than close to the center. This happens, if X-rays pass through the center of an object and penetration increases with traversed distance due to beam hardening. Another reason for such artifacts may be scattered radiation." [7]

**Motion artifacts** "Motion artifacts are caused by motion of the imaged object, which badly influence the sharpness of an imaging system. They manifest themselves as spreading of object boundaries and general blurring. While in CT it is possible to keep image acquisition time short and hence reduce patient's motion to a minimum, in CBCT it is not due to relative long acquisition times up to several minutes. These long acquisition times are caused by a limitation of the gantry speed due to International Electrotechnical Commission (IEC) regulations. Involuntary motion, forced by location of the desired object close to lung or heart, can cause severe problems in image quality in CBCT." [7]

### 4.1.2 Use of CBCT for Treatment Planning

CBCT is widely spread in radiotherapy, although the image quality is worse than at conventional CT, mainly caused by various artifacts (see section 4.1.1). Still enough anatomical information is provided to allow using CBCT as the basis for IGRT and adaptive radiotherapy. However, it is not possible to use CBCT images directly, without any additional adaption for online ATP, since the artifacts and the lower SNR the Houndsfield units (HU) do not match between CT and CBCT. Nonetheless, HU are needed in treatment planning systems and particularly in dose calculation algorithms because they imply density information of the tissue. To overcome this problem, in recent literature different methods were developed and presented.
For CBCT imaging on the LINAC two commercial devices are available, namely the OBI system (Varian Medical Systems, Palo Alto, CA) and the Synergy XVI system (Elekta, Crawley, UK). Although the basic devices are identical, there are some differences. Yoo and Yin [37] investigated the difference in HU between conventional CT and CBCT, profiles of Catphan phantom (The Phantom Laboratory, Incorporated, NY) and various tissue regions using an OBI system. The Catphan phatom is especially designed for quality assurance in three dimensions and contains different tissue equivalent and tissue substitute material inserts [7]. Additional the dosimetric consequence was investigated by comparing CBCT-based treatment plans to conventional CT-based plans for both phantoms and patients. They discovered that HU differences were lower than 10HU in all materials of the Catphan, except Teflon, where the difference was 34 HU. In addition in CBCT HU values decreased in the peripheral region compared to those in CT and scatter and artifacts in CBCT became severe near inhomogeneous tissues, with differences up to 200HU. However, the isodose distributions between CBCT-based and CT-based plans agreed very well, whereby the the discrepancy of isodose lines for both, 3D and IMRT plans, were bigger than the phantom based plans.
Richter et al. [26] further investigated the difference in HU and physical density by obtaining both, CT and CBCT images for 33 patients, namely 11 pelvis, 11 thorax and 11 head patients. In contrast to Yoo and Yin [37], they used

Synergy XVI for CBCT imaging. Additional influences of different image acquisition parameters such as tube voltage, filters and collimators were measured. Radiation therapy plans were calculated for CT and CBCT separately, and dose distributions compared. For different correction strategies CT HU values and density D in CBCT images were analyzed: standard CT HU-D table without adjustment for CBCT; phantom based HU-D tables; patient group based HU-D tables (pelvis, thorax, head); and patient specific HU-D tables. In *figure* 19 a HU-D table for CT as well as CBCT is presented.

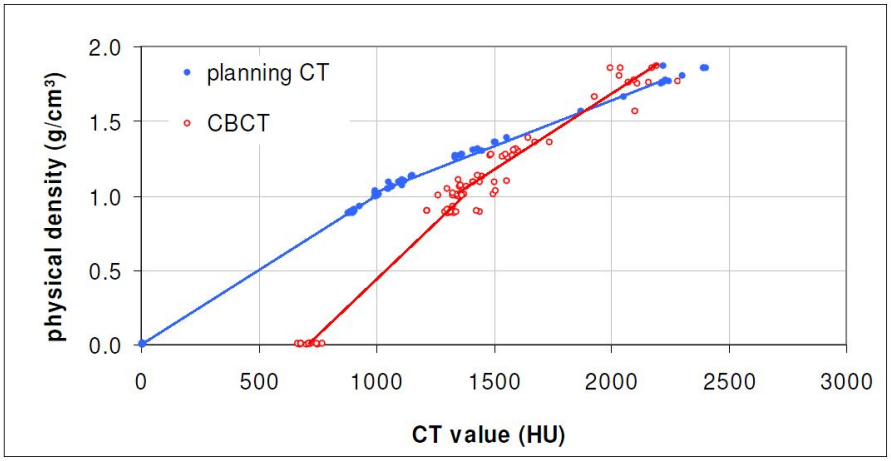


Figure 19: Generated HU-D tables for planning CT (blue) and group based CBCT (red) for pelvis patients [26]

They found large deviations of CT values between planning CT and CBCT for both, phantom and clinical CBCT studies. Hence the use of the default HU-D table for CT is associated with unacceptably inaccurate dose calculation in the CBCT studies. Additionally, HU values were highly influenced by the CBCT image acquisition parameters tube voltage, filtering and collimation, which suggests that a single HU-D table will not be applicable. Phantom based HU-D tables led to small errors in the cranial region, due to similar geometry, but were highly inaccurate for thorax and pelvis patients resulting in errors larger than 5% [5], which again shows the influence of the patient geometry on HU values in the CBCT. Between CBCT dose calculation with HU-D tables specific for the patient group or specific for each individual patient, errors were less than 5%. Consequently, once the patient group based HU-D tables are created, no reference data set such as a planning CT is needed for dose calculation and therefore plan adaption.

[5] 5% uncertainty in determination of CT scanner density will result in deviation of 1% in the calculated dose [26]

## 4.2 Adaptive planning workflow

### 4.2.1 Patient Selection

In this work 30 patient cases were selected for the retrospective evaluation of CBCT-based dose calculation in ART. Due to the availability of CT & CBCT images at the Medical University of Vienna, 10 cases were selected for prostate, lung and head and neck (H & N) tumors. Furthermore the high relation to clinical practice plays an important role in the selection of cases. According to Richter et al. [26] especially these three tumors are relevant sites for ART due to the high motion and tumor shrinkage. All dosimetric calculations were performed with a commercial version of XVMIC Monte Carlo algorithm implemented in the TPS iPlan 4.5 (BrainLab, Germany).
According to indications of the treatment approaches, the patients have been planned as the following:

- For prostate patients conventional 3DCRT and 7 beam IMRT plans are created. For 3DCRT 4 beams are used, placed at 0°, 90°, 180°and 270°("four-field box"). IMRT beams are placed equidistantly. As treatment machine Elekta Synergy Beam Modulator MLC 10MV is used, using 2Gy per fraction and 33 fractions (66Gy). Rectum, bladder and femoral heads are defined as organs at risk.

- For lung patients conformal 7 beam stereotactic body radiation therapy (SBRT) plans are created. Again, Elekta Synergy Beam Modulator MLC 10MV is used as treatment machine and 3 fractions with 15 Gy each are applied. Lung, oesophagus and spinal cord are defined as organs at risk.

- For head and neck patients 9 beam IMRT plans with simultaneous integrated boost (SIB) are created. Due to different geometric circumstances (in detail: the fieldsize is larger) Elekta Synergy MLCi 6MV is used as treatment machine and 30 fractions with 2 Gy (1.8 Gy) are applied to the patient. Parotid gland, brainstem and spinal cord are defined as OARs.

### 4.2.2 Planning and CBCT-based recalculations

In this section the basic workflow and the various steps to obtain the CT and CBCT plans are presented, based on the treatment planning system iPlan 4.5 (BrainLab). In this chapter only the planning itself, not the contouring of the organs by marking them slice by slice is presented. Firstly the general treatment planning process is presented in detail, using prostate cases as example. Secondly specific differences for treatment plans of lung and H & N are provided.

**Workflow for prostate- CT plans** After loading the CT image set, which includes the contours of all relevant organs of the patient, into the TPS program iPlan RT Dose 4.5, the default HU-ED table for conventional CT and a 3mm grid size has to be chosen (see *figure* 20).
A particular feature of prostate cancer treatments at the Medical University of Vienna is that an air filled rectum balloon is applied during image acquisition. Therefore some inhomogeneities arise during dose calculation at the overlap of PTV and rectal balloon. To overcome this problem an artificial density value is used to compensate artificial air voxels in this area. In detail a density of

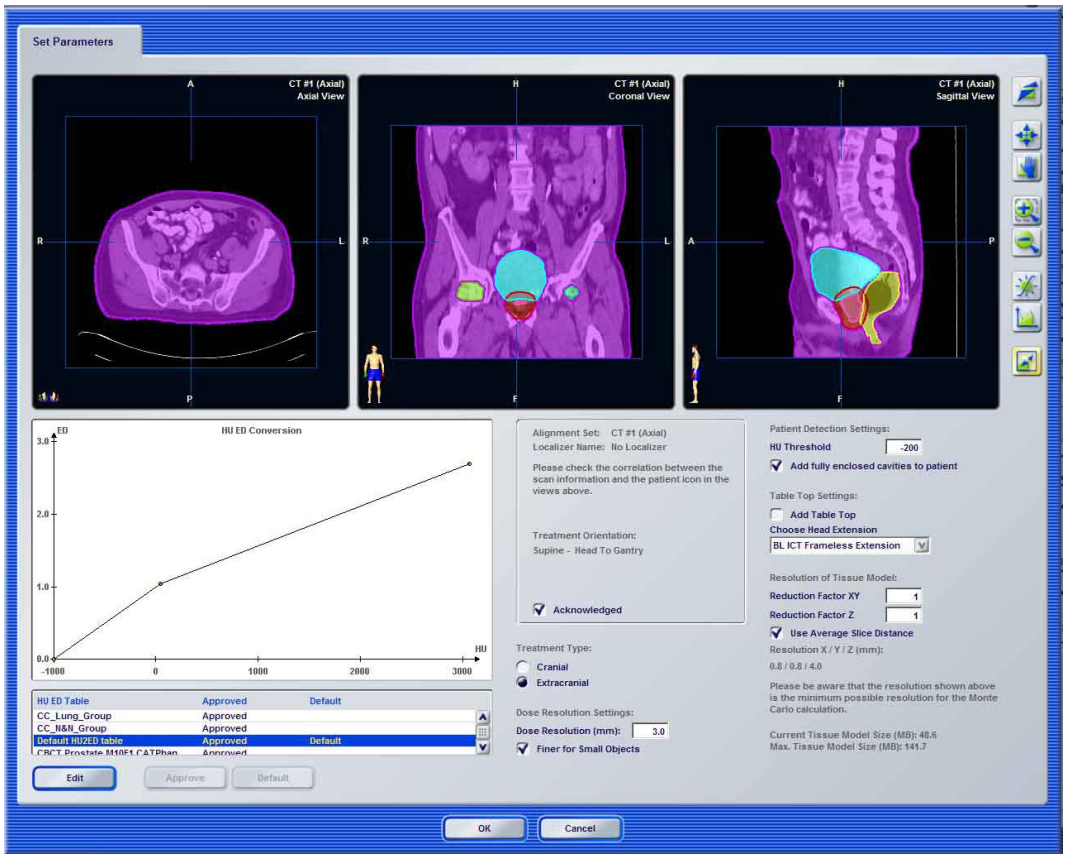


Figure 20: Selection of the standard HU-ED conversion curve

30HU is used due to the average natural prostate density. This corrections prevents artificial air voxels to manipulate and distort the optimization and dose calculation processes (see *figure* 21). Additionally CT scans for prostate patients are acquired with a contrast agent in order to distinguish the border between prostate and bladder. However, during treatment no contrast agent is used, which leads to wrong densities in planning CT images and furthermore to distortions in dose calculation. Hence bladder density should be overridden with its natural density, which can be approximated very well by the density of water (HU=0).

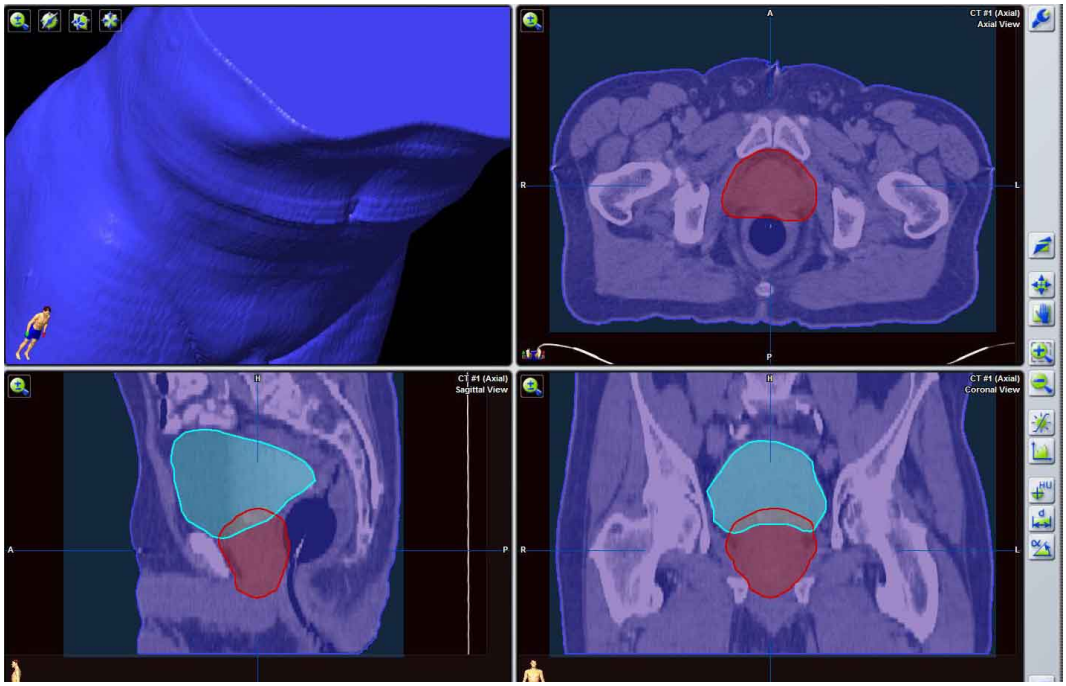


Figure 21: PTV- balloon intersection and bladder get homogeneous HU values for CT planning

In the next step the actual treatment plan has to be created by defining the PTV and the OARs. Therefore the previously defined structure "PTV" has to be defined as PTV in the TPS by checking the corresponding checkbox. The treatment dose and the number of fractions have to be set to 30 fractions with 2Gy each. Furthermore bladder and rectum have to be defined as organ at risk with the highest priority for dose calculation (OAR(1)), while femur has to be selected as low priority organ at risk (OAR(3)) (the number describes the priority of the constraints during dose calculations and optimization, see *figure* 22).
Afterwards numeric dose constraints for both, the PTV and the OAR have to be chosen for the optimization process as shown in *table* 1 and *table* 2.
In the next step a treatment unit (LINAC) which performs the treatment, has to be added in the TPS. For prostate cases an Elekta Synergy Beam modulator Linac with 10MV is used (see section 4.2.1). According to the type of treatment an IMRT beam has either be selected or not. For prostate IMRT plans an IMRT

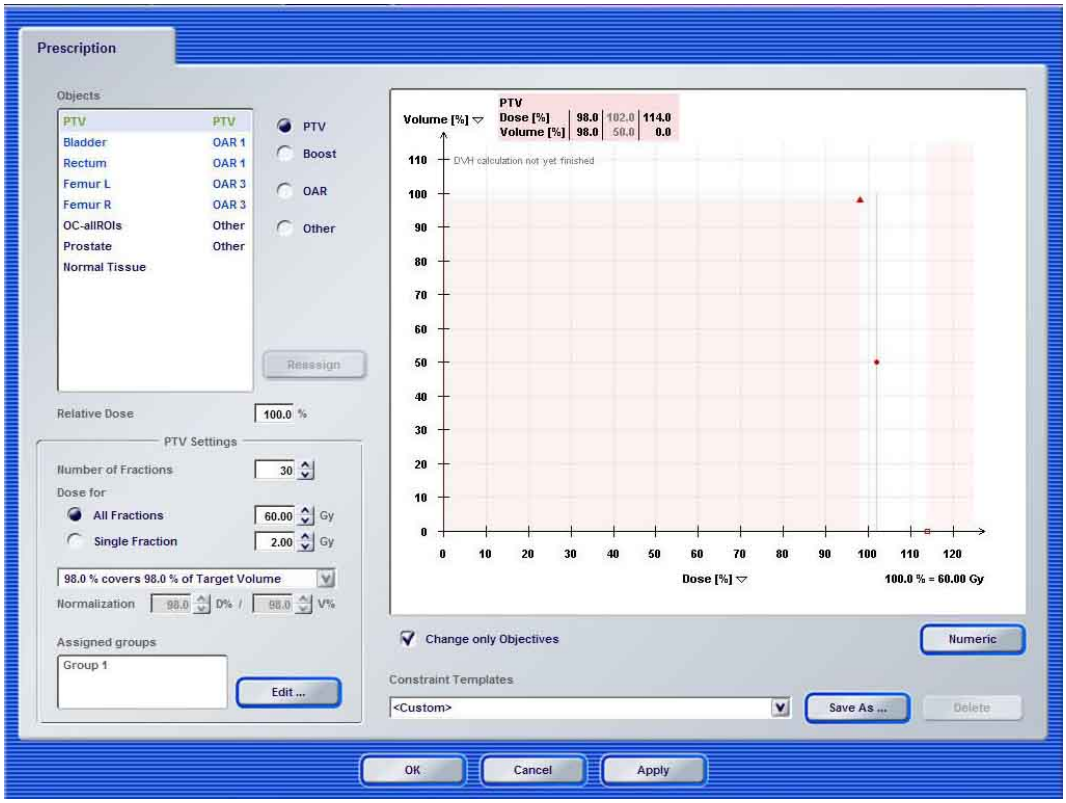


Figure 22: Definition of PTV and OARs, according to their priority in the prescription dialog.

Table 1: Numeric dose constraints for PTV. Prescribed dose is 100% equal.

| PTV | |
|---|---|
| Dose (%) | Volume (%) |
| 114 | 0 |
| 98 | 98 |
| 102 | 50 |
| 0 | 100 |

Table 2: Numeric dose constraints for OARs, namely rectum, femur and bladder. 100% indicates prescribed dose to PTV.

| Rectum | | Femur | | Bladder | |
|---|---|---|---|---|---|
| Dose (%) | Volume (%) | Dose (%) | Volume (%) | Dose (%) | Volume (%) |
| 100 | 0 | 50 | 0 | 103 | 0 |
| 80 | 10 | 20 | 20 | 80 | 20 |
| 60 | 20 | 10 | 50 | 60 | 30 |
| 40 | 50 | 5 | 70 | 40 | 50 |
| 0 | 100 | 0 | 100 | 0 | 100 |

beam with 3mm collimator margin around the PTV and 7 elements (number of beams in the plan) are selected (see *figure* 23).

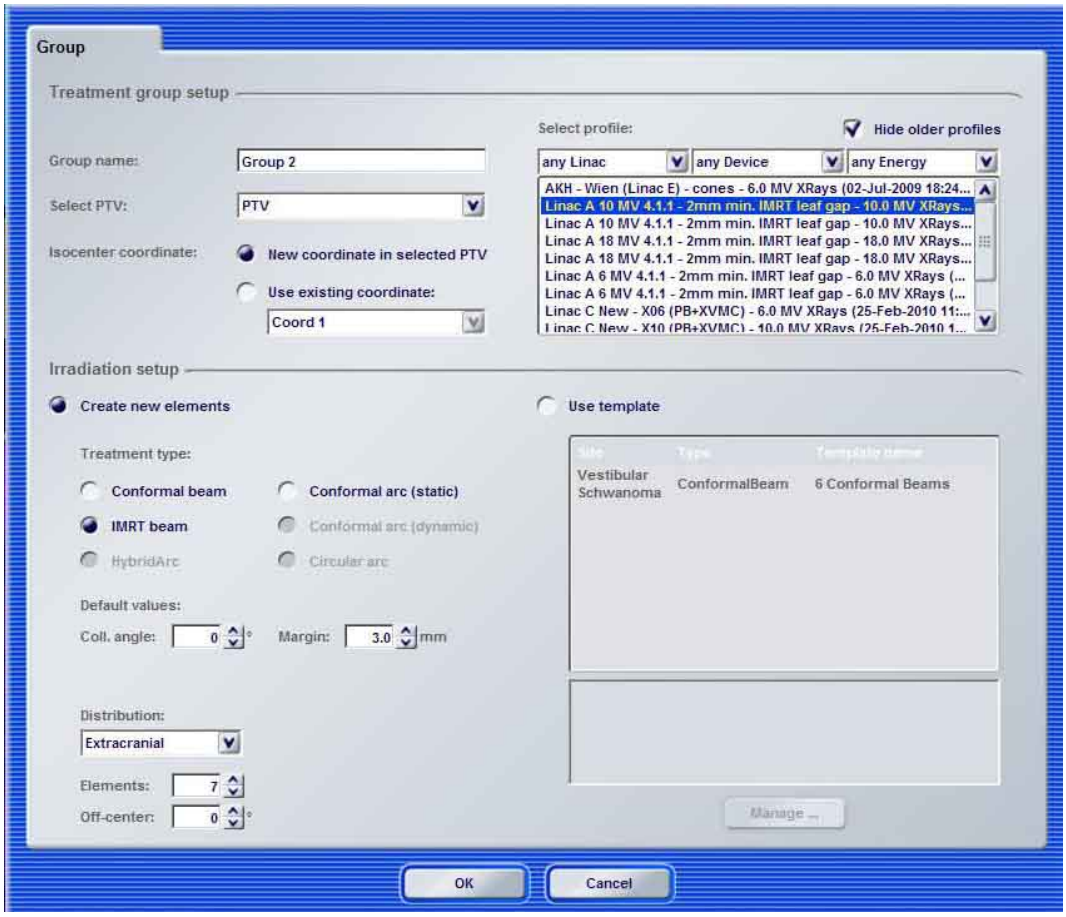


Figure 23: Selection of treatment group dialog

In order to shield rectum more efficiently, the position of beams was re-arranged from default (starting at 0°) to a sequence starting at 180°. After defining the treatment plan parameters, iPlan continuous with an IMRT dose optimization dialog. Parameters for the dose calculation grid and the beamlet size for optimization (both 3mm) and maximum number of segments in a field (15) have to be entered (see *figure* 24).
Finally the program provides different optimizations process outcomes, according to the consideration of the OAR constraints. In detail, there are four different options available. "PTV only" does not consider OARs at all in the dose optimization process and simply optimizes to fulfil PTV constraints previously defined. In contrast to that, "OAR low", "OAR medium" and "OAR high" include dose constraints for OARs in the optimization process as well. As the name already suggests, "OAR low" puts the priority in dose optimization on PTV constraints, while "OAR high" puts the focus also on OAR constraints. Mostly "OAR high" or "OAR medium" provides the best results concerning

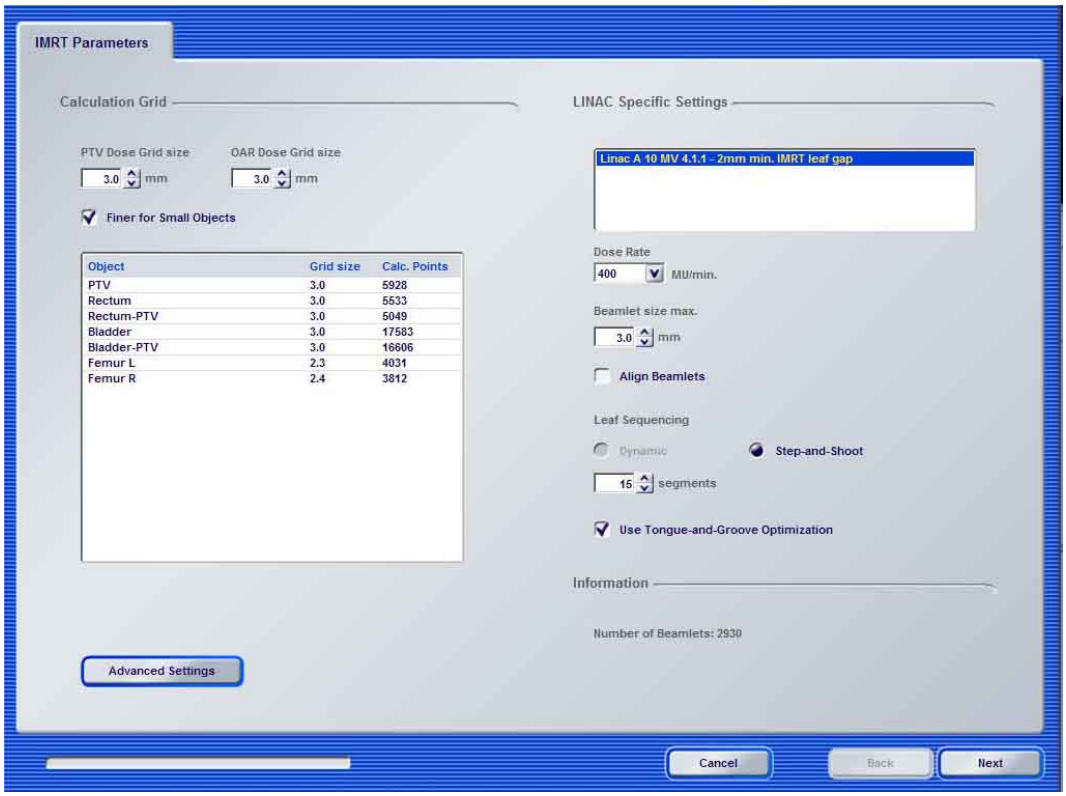


Figure 24: Definition of IMRT optimization parameters dialog

sparing of OAR and coverage of PTV. In the last step the Monte Carlo optimization has to be performed to maintain the final dose calculations.

**Workflow adaptions for prostate 3DCRT plans** In contrast to prostate IMRT plans a conformal beam with a collimator margin of 8mm is used for 3DCRT plans. Four beams spaced at 90°and starting at 0°are used. Numeric constraints are used just for PTV and are shown in *table* 3.

Table 3: Numeric dose constraints for PTV. 100% indicates prescribed dose to PTV.

| PTV | |
|---|---|
| Dose (%) | Volume (%) |
| 95 | 95 |
| 100 | 50 |
| 107 | 0 |

**Workflow adaptions for lung cases** Lung cases are planned with 7 conformal beams and a margin of 0mm. The dose per fraction is 15Gy and 3 fractions are applied. Another major difference is that no inverse treatment planning procedure is applied and therefore only one prescription is selected: 65% of the applied dose have to cover the PTV. To spare as much healthy lung tissue as possible, the 7 beams are manually placed around 180°- 200°arc on the tumor side, leading to decreased doses at OARs.

**Workflow adaptions for head and neck cases** Due to simultaneous integrated boost strategy (SIB) for the selected patient cases, two PTVs are selected for H & N cases. While the lymphatic tissue on tumor side is irradiated with a dose of 60Gy (PTV60), lymphatic tissue on the opposite side is irradiated with a lower dose (50Gy, PTV50) to avoid possible metastases in the future. 28 fractions are applied with 2 and 1,8Gy per fraction for PTV60 and PTV50, respectively. Brain stem, parotid gland (side of PTV50) and myelon, are classified as OAR with highest priority (OAR1). The constraints for PTV and all OAR are presented in *table* 4 and *table* 5.

Table 4: Numeric dose constraints for PTV. Maximum dose (100%) is 50/60Gy for respective PTVs

| PTV50 | | PTV60 | |
|---|---|---|---|
| Dose (%) | Volume (%) | Dose (%) | Volume (%) |
| 120 | 0 | 107 | 0 |
| 98 | 98 | 98 | 98 |
| 102 | 50 | 104 | 50 |

Additional a different treatment machine (6MV LINAC Synergy MLCi) is used due to larger field size and the necessity to irradiate targets in close proximity to the skin. An IMRT beam with 9 beams is used, including a dose calculation grid size of 3mm, a beamlet size of 10mm and 18 segments. Due to the high amount of data in H & N cases, dose calculation grid for normal tissue is reduced

Table 5: Numeric dose constraints for OARs, namely brain stem, parotid gland and myelon.

| Brain Stem | | Parotid gland | | Myelon | |
|---|---|---|---|---|---|
| Dose (%) | Volume (%) | Dose (%) | Volume (%) | Dose (%) | Volume (%) |
| 45 | 0 | 60 | 0 | 45 | 0 |
| 40 | 10 | 50 | 10 | 40 | 10 |
| 0 | 100 | 25 | 35 | 0 | 100 |
| - | - | 0 | 100 | - | - |

to 8mm, otherwise the TPS collapses. Additionally a margin around PTV is selected (10mm) where a proper dose gradient can be achieved.

**Workflow for prostate- CBCT plans** To create CBCT plans, the previously created planning CT treatment plan has to be finished and saved. To simplify subsequent work with the CBCT image set, additional structures, like outer contour minus all ROIs ("OC-AllROIs") and outer contour minus rectal balloon and femur ("OC-ballon-FH") are created by simple structure subtraction in iPlan.
The general workflow is the same for all CBCT plans: CBCT structures are opened in the BrainLab Phantom QA module, afterwards the corresponding CT plan is loaded. Due to imaging principle differences between planning CT and CBCT the nominal isocenter of both techniques not the same. This is fixed by simple translation of the treatment group into the focus of the PTV.

**Population-based conversion curve** The population- based conversion curve is based on HU values of each patient group and was already discussed in literature [26] [37]. In both, CT and CBCT data sets various ROIs with different densities are contoured. This process is done for every patient in the corresponding group (e.g. for all 10 prostate cases). After the mean HU value for each ROI is calculated in CT and CBCT data sets, a HU-ED conversion curve (CC) is calculated. As already mentioned before this process has to be done for each group of cases.
To chose the population-based conversion curve, the menu for surface segmentation is selected. After hitting the "set parameters" button a new windows opens and the correct conversion curve can be selected. Again a grid size of 3mm is selected.

**Phantom-based conversion curve** This approach was already discussed in the work by Hopfgartner [7]. The essential idea is similar to the population-based conversion curve approach. However, instead of various densities obtained by patient images, the conversion curve is based on CT and CBCT images of the CATPhan phantom, which contains different tissue equivalent and tissue substitute material inserts.

**Water-air-bone** In contrast to the previously discussed approaches of CBCT dose calculations, here the standard CT HU-ED conversion curve is

used. The conversion of HUs into densites is done by assigning three densities to various structures. In detail, bone (hard bone = 400HU, soft bone = 250HU), the rectum balloon (air equivalent = -1000HU) and the normal tissue including the tumor (water equivalent = 0HU) are manually overridden (see *figure* 25).

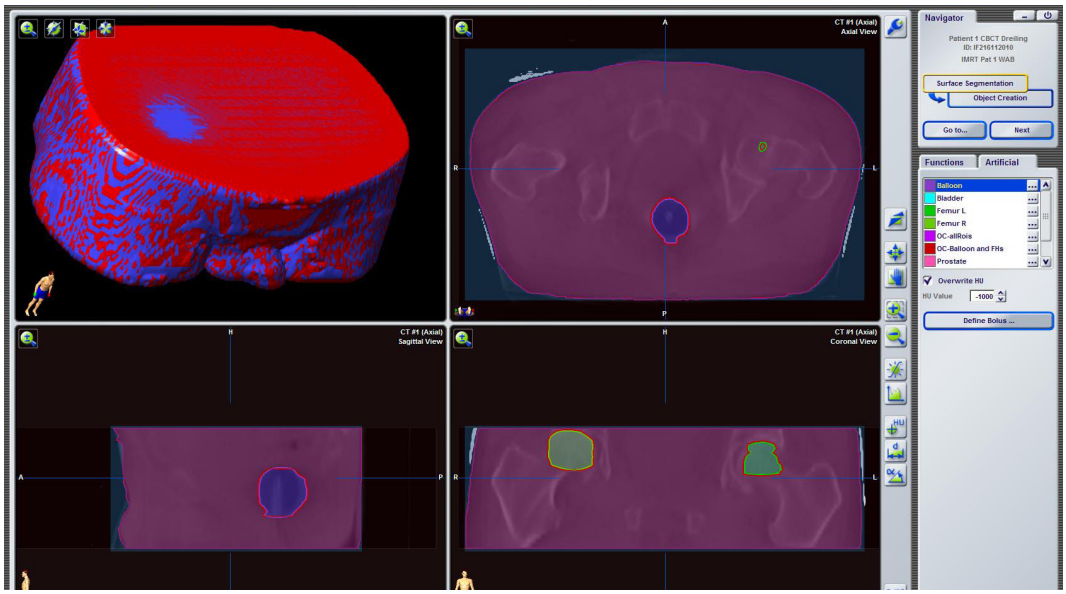


Figure 25: Overwrite three structures with WAB values

**ROI mapping** Again the standard CT conversion curve is used. However, instead of assigning only 3 distinct values for all ROIs, mean HU values for each structure and patient of planning CT images are calculated. These values are used to replace native densities of the CBCT data-sets.
Afterwards dose calculation is performed on CBCT data-sets.

**Workflow adaptions for lung cases** For the phantom based and the population based conversion curve approach the workflow is identical to prostate cases. However, the selection of the correct HU-ED conversion curve is crucial for reliable results. For the WAB approach different structures are overridden, namely bone (including ribs = 250HU), lung (-750HU), normal tissue (0HU) and PTV-lung overlap (-600HU). For the ROI mapping approach, again all structures are overridden by the corresponding mean HUs of the planning CT image-set.

**Workflow adaptions for head and neck cases** For population based and phantom based conversion curve the corresponding conversion curves have to be selected. For ROI mapping also all structures of the CBCT have to be overridden by the corresponding CT values. At WAB approach 6 structures are artificially replaced: Body- Air and Bone (0HU), bone soft (250HU), base of scull (not in all cases, depends on the tumor position, 650HU), bone teeth (1000HU), air (-1000HU) and headsupport pillow (-850HU).

## 4.3 Comparison strategies

### 4.3.1 DVH parameters

Dose volume histograms (DVH) provide a commonly used tool to evaluate treatment plans and form the basis of current IMRT optimization approaches employed for inverse planning [2]. The "volume" referred to in the term dose volume histogram can either be a target of radiation treatment, a healthy organ nearby a target or an arbitrary structure. Due to the cumulative structure it is possible to obtain nearly every parameter needed. The TPS iPlan provides DVHs for every OAR and also for PTVs automatically which makes it easier to evaluate data and enables export als ".txt" file. In addition to various maximum, mean and median doses also organ coverage especially for PTV is strongly used due to the high amount of information. In *figure* 26 a DVH in iPlan is presented.

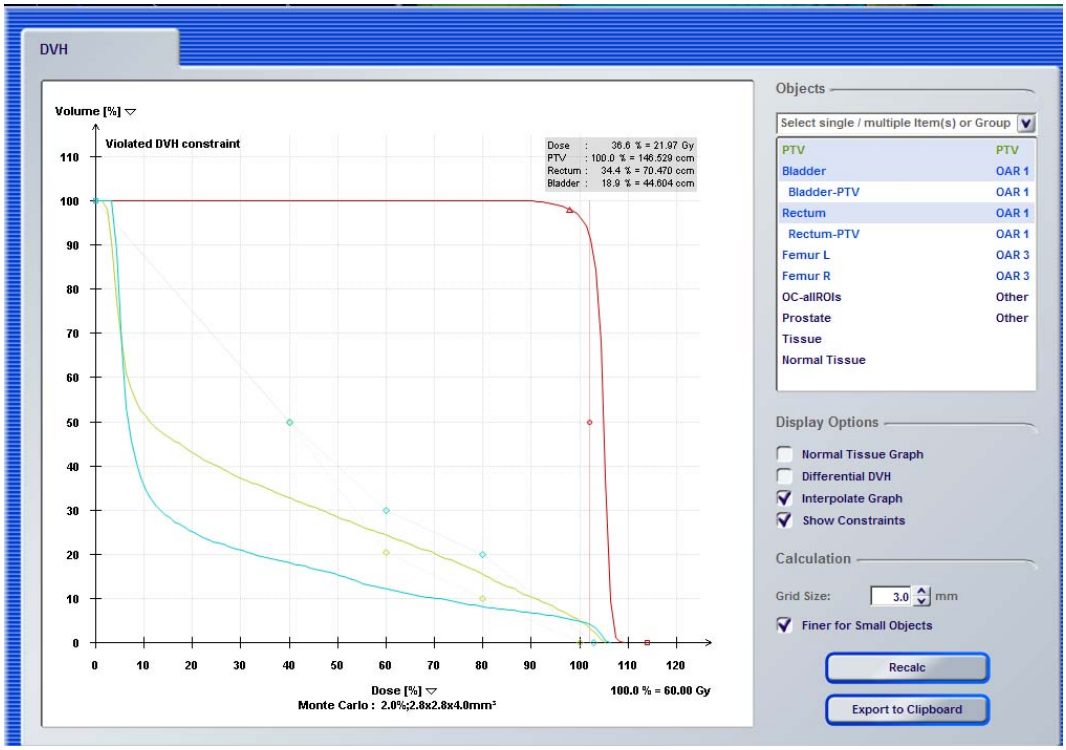


Figure 26: Dose volume histogram (DVH) for PTV in iPlan

According to ICRU guidelines for IMRT evaluation we used the following parameters for our study:

- PTV mean dose
- PTV max dose
- PTV median dose
- PTV dose for 98% volume coverage

- PTV dose for 2% volume coverage
- CTV median dose
- CTV mean dose
- Maximum and mean doses for OARs

### 4.3.2 Gamma evaluation

As conformal radiotherapy and IMRT are complex techniques, the use of methods capable of assessing the quality of competing treatment plans and verifying their dosimetric accuracy has been strongly recommended [31]. Furthermore the comparison of the evaluated dose distribution to the planned distribution is essential for successful radiotherapy [6]. One method for quantitative evaluation of dose distributions through a composite analysis of distance-to-agreement (DTA) and dose difference (DD) was 1998 presented by Low et al. and is called "$\gamma$-evaluation" [16] [31]. It incorporates pass- fail criteria for both DTA and DD, resulting in a numerical index ($\gamma$) as a measure of the agreement between two datasets [31].
In detail the parameters for evaluation are the dose difference $\Delta D_M$ between the measured and a calculated dose in a certain point and distance-to-agreement ($\Delta d_M$), which is the distance between a measured data point and the nearest point in the calculated dose distribution that has the same dose [6]. Mostly used criteria values in literature are 3 mm for the DTA and 3% (of the dose to normalization point) for the dose difference [6]. Gamma evaluation can be used to compare two dose distributions in general. Nonetheless, in clinical practice it is often used to compare a calculated to a measured dose distribution. However, in this work two calculated dose distributions are compared.
Evaluation for a single measurement point $\vec{r_m}$ is presented in *figure* 27.
Fotina [6] explains the calculation of $\gamma$-value, described by Low et al. [16] and $\gamma$- angle, described by Stock et al. [32], as the folling:
"The $\delta$-axis represents the difference between the measured dose$[D_m(\vec{r_m}]$ and the calculated dose $[D_c(\vec{r_c})]$. The $x$- and $y$-axis represent the spatial location $\vec{r_c}$ for the calculated distribution relative to a measured point. The vertical line with a length of $2\Delta D_M$ represents the dose difference test. If the calculated dose distribution surface crosses the line $[D_c(\vec{r_m}) - D_m(\vec{r_m}) < \Delta D_M]$, the calculated distribution passes the dose difference test at the measurement point $\vec{r_m}$.The DTA criterion, $\Delta d_M$, is represented by a disk in the $\vec{r_m} - \vec{r_c}$ -plane with a radius of $\Delta d_M$. If the calculated dose distribution surface, $D_c(\vec{r_c})$, intersects the disk, the DTA is within the acceptance criterion and the calculated dose distribution passes the DTA-test at that point.
Defining the acceptance criteria not just along the $\delta$-axis and in the $\vec{r_m} - \vec{r_c}$ -plane allows a more general comparison between calculation and measurement than the traditional composite evaluation does. Thus an ellipsoid is selected as the surface defining the new criterion. The equation that defines this surface is:

$$\sqrt{\frac{r^2(\vec{r_m}, \vec{r_c})}{\Delta d_M^2} + \frac{\delta^2(\vec{r_m}, \vec{r_c})}{\Delta D_m^2}} = 1 \tag{1}$$

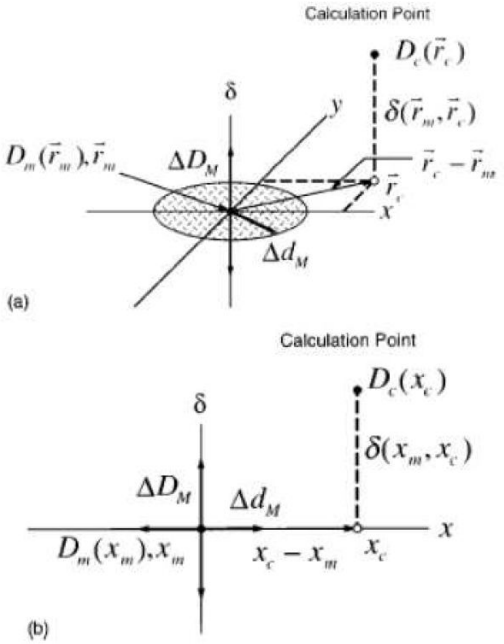


Figure 27: Geometric representation of dose distribution evaluation criteria for the dose difference and DTA tests, (a) two-dimensional representation, (b) analogue one- dimensional representation [16]

with the distance between the measured and the calculated dose

$$r(\vec{r_m}, \vec{r_c}) = |\vec{r_c} - \vec{r_m}| \tag{2}$$

and the dose difference at point $\vec{r_m}$

$$\delta(\vec{r_m}, \vec{r_c}) = D_c(\vec{r_c}) - D_m(\vec{r_m}) \tag{3}$$

If any portion of the calculated dose distribution surface $[D_c(\vec{r_c})]$ intersects the ellipsoid, the defined criterion is fulfilled at $\vec{r_m}$. Based on this terminology, the $\gamma$-index, which is the minimum distance between the measurement point under investigation and all points of the calculated distribution, is calculated as follows:

$$\delta(\vec{r_m}) = min\,\{\Gamma(\vec{r_c}, \vec{r_c})\}\,\forall\,\{\vec{r_c}\} \tag{4}$$

with

$$\Gamma(\vec{r_m}, \vec{r_c}) = \sqrt{\frac{r^2(\vec{r_m}, \vec{r_c})}{\Delta d_M^2} + \frac{\delta^2(\vec{r_m}, \vec{r_c})}{\Delta D_m^2}} \tag{5}$$

The ellipsoid represents the surface of the combined acceptance criteria (see *figure* 28). Mathematically it can be expressed as

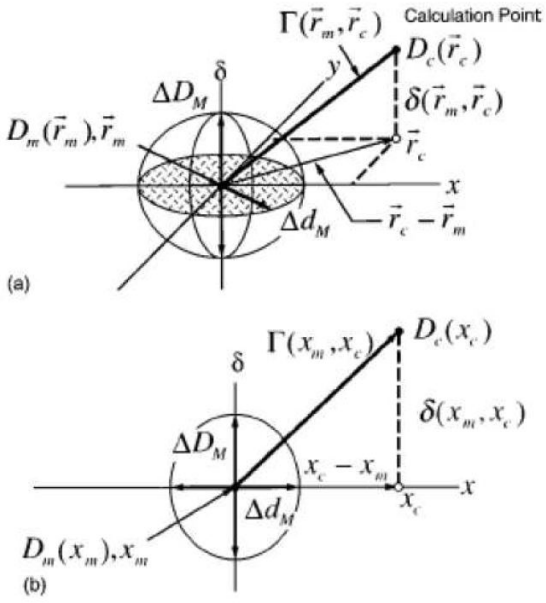


Figure 28: Geometric representation of dose distribution evaluation criteria using the combined for the dose-difference and DTA test; (a) two-dimensional representation, (b) analogue one-dimensional representationn [16]

$$\gamma(\vec{r_m}) \leq 1 \tag{6}$$

Next to the $\gamma$-index, also the $\gamma$-angle is considered to be a very useful tool for the interpretation of dose distributions. The $\gamma$-angle indicates the parameter mostly influencing the $\gamma$-index, the dose difference or the DTA. If the $\gamma$-angle is between 0 and $\pi/4$ the $\gamma$-index is dominated by the dose difference, if between $\pi/4$ and $\pi/2$ the $\gamma$-index is dominated by the DTA. The angle is calculated with the absolute values of dose difference and distance difference and thus always is in between 0 and $\pi/2$.
For a comfortable evaluation, it is preferable to graphically display the $\gamma$-index distribution as well as the $\gamma$-angle distribution. In addition, it is possible to statistically evaluate the $\gamma$- values by means of histograms."
Based on the experience during IMRT treatments at the Medical University of Vienna, Stock et al. [32] developed an evaluation filter for any IMRT hybrid plan verification based on a $\gamma$- vector analysis.

### 4.3.3 Conversion program for $\gamma$-evaluation

As already mentioned a program written by Markus Stock [6] was used to perform $\gamma$-evaluation in this work. This program was initially developed to perform comparisons, including dose-subtraction to see dose differences and $\gamma$-evaluation of simulated dose distributions, exported from the TPS, with real results obtained by digital films placed in a irradiated phantom. However, for an evaluation of two exported slices of the TPS, some incompatibility problems were revealed due to different file structures of the exported files. Therefore I wrote a program in Matlab which converts exported files of BrainLab into compatible files for evaluation.
The program distinguishes between "CT-files" on the on hand (left side of the program window) and "Film-files" on the other hand (right side of the program window). In *figure* 29 a screenshot of the program used for evaluation is presented.

In the section A two conversion programs for both, "CT-files" and "Film-files" are presented. The files are always named in the same scheme: P<patient number><CT or CBCT1 - CBCT4><iso or +- mm>, for example "P1CBCT3iso" or "P7CT+16mm".

[6] Markus Stock, Department of Radiotherapy and Radiobiology, AKH Vienna, Medical University Vienna, Vienna, Austria

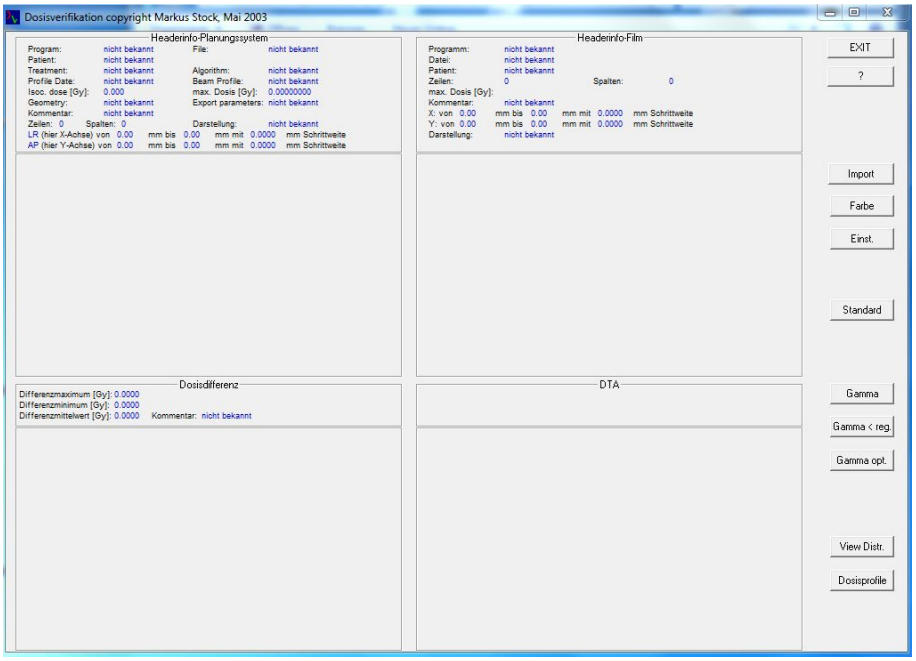


Figure 29: Screenshot of the evaluation program developed by Markus Stock. The exported file of the TPS is placed on the left side, the slice of the film is on the right side

# 5 Results and Discussion

This chapter is divided into three parts. In the first part all different HU-adjustment approaches are compared to the population-based conversion curve method, which is selected as "golden standard", due to high reliability and accuracy described in literature. The comparison is performed by evaluating dose-volume-histograms (DVHs) for PTV and OARs. In the second part $\gamma$-evaluation is performed for all CBCT approaches. Again, the population-based conversion curve approach is selected as reference. In the third part the two best performing HU-adjustment techniques are compared to CT data. Additional some sample cases where extreme dose deviations were observed are illustrated. In the following section tables show values as the following: median value in front, mean value and standard deviation in brackets (Median [Mean ± SD])

## 5.1 DVH- Analyzes

### 5.1.1 Prostate cases

For 4FBox plans for prostate cases strong differences in PTV coverage were observed (variations between 53.7% and 100%). Also median PTV dose showed deviations between 94,9% and 103%. Especially PTV coverage, which is presented in *figure* 30, shows a very large standard deviation for the phantom based conversion curve method in contrast to the other approaches.

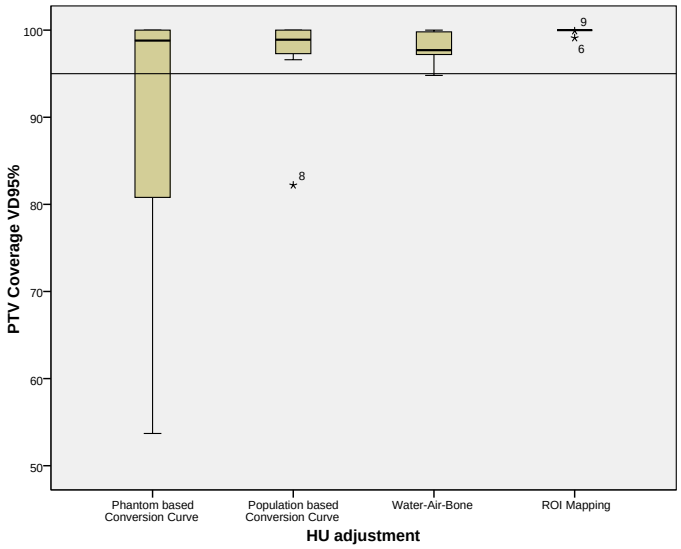


Figure 30: PTV Coverage for 10 prostate cases obtained with different CBCT plan approaches.

Median values for PTV coverage were 98.8%, 98.9%, 97.7% and 100% for the

phantom- based conversion curve-(CC), population- based conversion curve-(CCP), water-air-bone- (WAB) and ROI mapping approach(ROI), respectively. However, 95% PTV coverage as a criterion for plan quality was fulfilled for every patient only for the WAB and the ROI mapping techniques.
For median PTV doses also the phantom- based conversion curve method shows comparable results, concerning statistical distribution, as shown in *figure* 31.

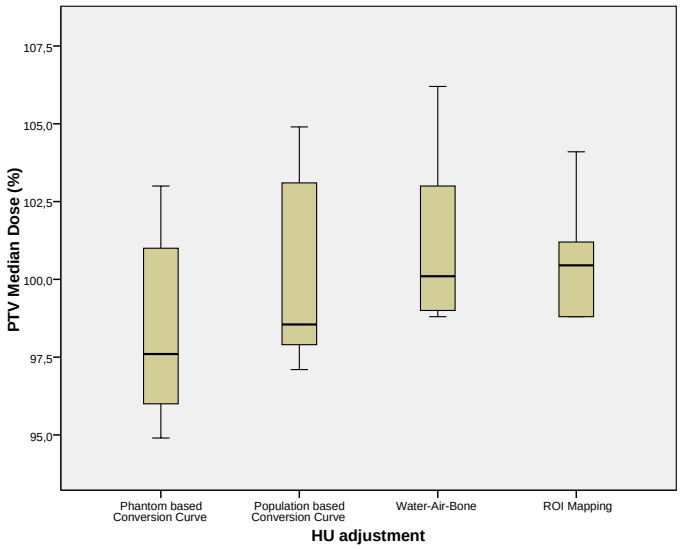


Figure 31: Median PTV dose for prostate cases in % of prescribed dose.

Nonetheless, both conversion curve based methods showed a lower median dose than the WAB and ROI mapping approaches, namely 97.6% and 98.6% versus 100.1% and 100.5% of the prescribed dose.
In *table* 6 mean and median values as well as standard deviation for organs at risks are shown.

Table 6: Median doses for organs at risk in % of prescribed dose for the 4FBox prostate plans for all patients.

| | CC | CCP | WAB | ROI |
|---|---|---|---|---|
| Rectum $D_{Max}$ | 100.9 [99.9±5.7] | 101.9 [102.7±3] | 101.5 [102.7±3.6] | 101.9 [102.8±2.6] |
| Rectum $D_{Mean}$ | 61.7 [60.6±14.4] | 62.9 [61.2±14.2] | 62.6 [61±13.6] | 63.5 [61.7±14.1] |
| Bladder $D_{Max}$ | 99.8 [100.2±3.2] | 101.5 [102.5±3] | 103.3 [103.8±3.1] | 101.3 [101.9±2.2] |
| Bladder $D_{Mean}$ | 38.3 [41.9±20.4] | 39 [42.6±20.7] | 39.9 [43.7±21.4] | 39.8 [43±20.8] |

Both conversion curve based methods showed systematically lower dose values than the WAB and ROI mapping approaches. Additionally, mean doses showed larger ranges than maximum doses for both, rectum and bladder. The phantom-based conversion curve technique showed the smallest median and mean doses

for bladder and rectum compared to the other methods. The WAB approach showed higher mean (0.7% and 1.1%) and median (1.7% and 0.8%) doses for maximum and mean bladder dose compared to the golden standard, the CCP method. The ROI mapping technique showed lower median and mean values compared to the CCP approach for maximum bladder dose (-0.2% and -0.6%). However, for mean bladder dose the ROI mapping approach overestimates median and mean doses by 0.8% and 0.4%, respectively.

PTV coverage values for IMRT planned prostate cases are presented in *figure* 32.

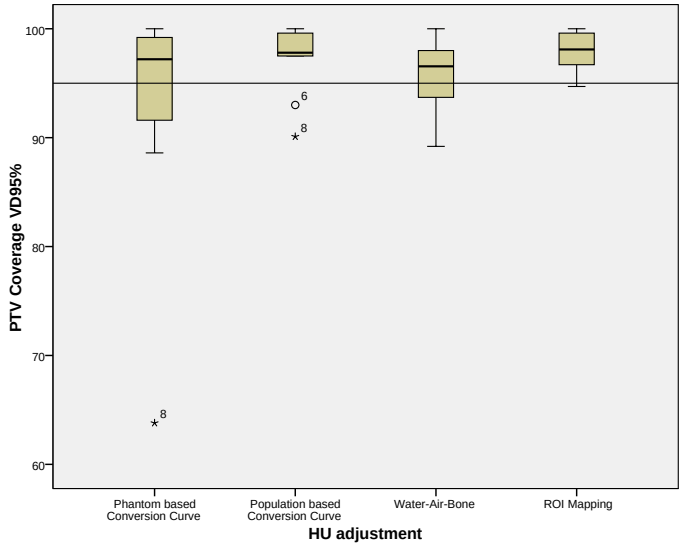


Figure 32: PTV coverage for IMRT planned prostate cases.

Again, the phantom- based conversion curve method showed, together with the water-air-bone method, the largest range. In contrast to that, the population-based CC technique showed extremely small ranges between 25% and 75% percentile. However, due to the small range two cases were marked as outliers with PTV coverage below the 95% criterion. For IMRT plans all methods showed cases with PTV coverage below 95%, the phantom- based conversion curve approach showed absolutely lowest coverage with 63.8% and 88.6% for patient 8 and 6, respectively. The most constant method was the ROI mapping technique with a PTV coverage above 95% for all cases, only patient 9 showed a PTV coverage slightly below 95% (94.7%).
Median PTV doses for IMRT planned prostate cases are shown in *figure* 33.
Obviously the range of values was larger for both conversion curve based methods compared to the WAB and ROI mapping techniques. Nonetheless, median dose varied just by 2% between 103% and 105% for all methods. However, only the WAB and ROI mapping techniques showed a median PTV dose above 100% of the prescribed dose for all cases.

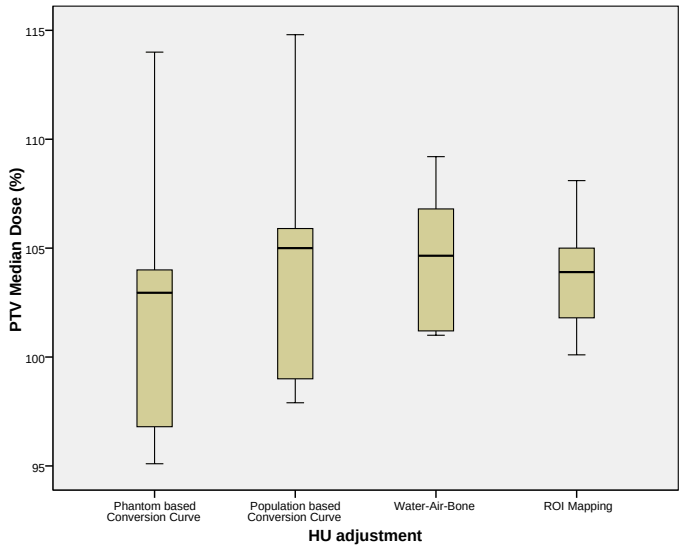


Figure 33: Median PTV dose for 10 patients using IMRT based plans.

In *table* 7 mean and median organs at risk doses for IMRT prostate plans are presented.

Table 7: Median doses for organs at risk in % of the prescribed dose for IMRT prostate plans.

| | CC | CCP | WAB | ROI |
|---|---|---|---|---|
| Rectum $D_{Max}$ | 104.3 [104.6±5.4] | 106.4 [106.6±5,1] | 105.7 [106.3±3.8] | 106.3 [106.8±3.5] |
| Rectum $D_{Mean}$ | 48.9 [48±8.5] | 49.8 [48.9±8.7] | 49.7 [49.2±9.1] | 49 [48.7±8.4] |
| Bladder $D_{Max}$ | 105.8 [105.6±6] | 106.7 [107.3±5.8] | 108.1 [108.2±4.1] | 106.3 [107.3±3.6] |
| Bladder $D_{Mean}$ | 32.6 [36±17.3] | 33.1 [36.5±17.6] | 33.8 [36.8±17.8] | 33.7 [36.7±17.8] |

The phantom- based conversion curve showed lowest median and mean doses for all OARs, except the mean dose of rectum where the ROI mapping technique showed a lower median value. Again, the statistical range for mean doses was higher than for maximum doses. Furthermore the CC and CCP approaches showed higher ranges for maximum doses compared to the WAB and ROI techniques. Only for the phantom- based conversion curve method, maximum rectum dose for single cases were below 100% of the prescribed dose. Additionally, all dose values of the CC technique were always below the dose values of the CCP, WAB and ROI mapping techniques, for nearly every single patient and all OARs. In more detail, the CC method underestimated OAR doses by an average value of 2.2%, 0.9%, 0.9% and 0.5% for maximum rectum dose, mean rectum dose, maximum bladder dose and mean bladder dose, respectively compared to the CCP approach. The WAB and ROI mapping techniques underestimated doses for maximum and mean rectum doses in a range between 0.1% and 1.4%

compared to the CCP method. However, mean bladder dose was overestimated by both, the WAB and ROI mapping approaches by 0.7% and 0.6% respectively, compared to the CCP technique. Maximum bladder dose was overestimated by the WAB approach (1.4%) and slightly underestimated by the ROI method (0.4%).

### 5.1.2 Lung cases

PTV coverage for 65% of prescribed dose is presented in *figure* 34.

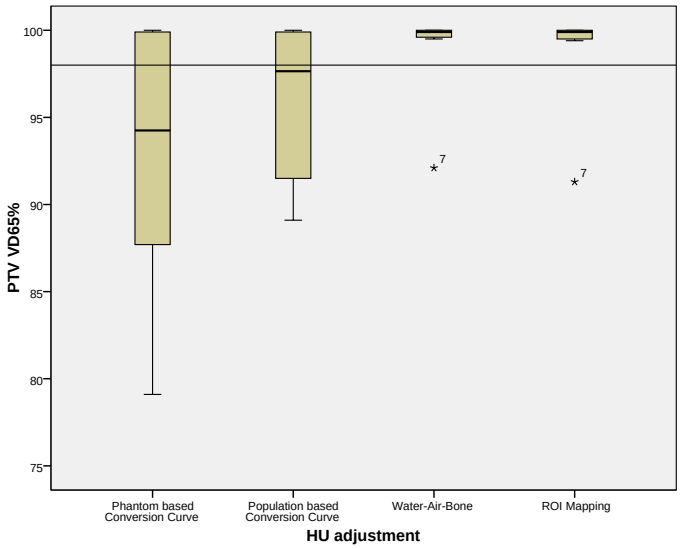


Figure 34: PTV coverage for 65% of prescribed dose at 3D SBRT lung plans.

The water-air-bone and ROI mapping approaches showed significantly smaller ranges of values for PTV coverage. Additionally median PTV coverage was clearly above 98% with values of 99.9% for both, the WAB and the ROI mapping approach. In contrast to that, median PTV coverage was 94.3% and 97.7% for the phantom- based conversion curve and population- based conversion curve methods, respectively. Patient 7 showed very low values for all methods, resulting in an outlier for both, the WAB and ROI mapping technique. However, if case 7 is ignored only non conversion curve based methods showed coverage above 98% for all cases.
Also for median PTV doses differences between the conversion curve based methods and non conversion curve based methods were obvious: the statistical range was larger and the median value was lower the for the CC and CCP approaches. Values for median PTV dose were 84.4%, 87.5%, 92.3% 91,9% of the prescribed dose for the phantom-based conversion curve, population- based conversion curve, water-air-bone and ROI mapping techniques. Like PTV coverage, PTV median dose also showed minima for case 7, although the differences were not as significant. Median PTV doses for 3D SBRT plans are presented in *table* 35.

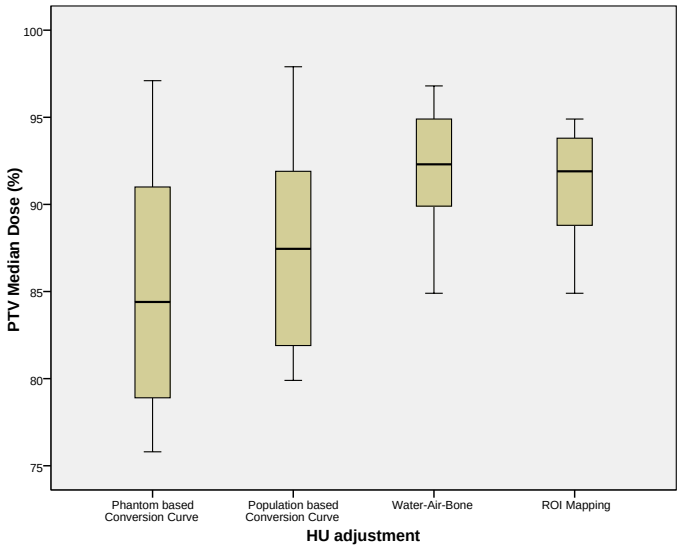


Figure 35: Median PTV doses for 10 lung cases.

Table 8: Median doses for organs at risk in % of prescribed dose for 3D SBRT lung plans.

| | CC | CCP | WAB | ROI |
|---|---|---|---|---|
| Spinal Cord $D_{Max}$ | 22.3 [18.4±6.3] | 22.3[18.1±6.5] | 21.2 [18±6.5] | 21.4 [18.2±6.4] |
| Esophagus $D_{Max}$ | 13.4 [17±7.1] | 13.4 [17±7.2] | 13.6 [17±6.9] | 13.5 [16.9±6.8] |
| Lung $D_{Max}$ | 103.1 [102±4.4] | 103.5 [102.4±3.9] | 102.1 [102.2±4.8] | 103 [101.9±3.9] |
| Lung $D_{Mean}$ | 8.7 [9.2±3.8] | 8.8 [9.2±3.9] | 8.8 [9.2±3.9] | 8.9 [9.3±3.9] |

For organs at risk doses no obvious differences between the conversion curve based and non conversion curve based methods could be detected. In contrast to prostate OAR doses, the statistical ranges were quite identical between the CC, CCP, WAB and ROI mapping approaches, with ranges between 3.8% and 7.2%. However, the WAB and ROI mapping approaches provided slightly smaller statistical ranges for maximum esophagus dose, whereas median and mean values were comparable. In more detail, the CC approach underestimated maximum lung and mean lung doses by 0.3% and 0.1%, respectively compared to the CCP technique. For maximum doses of spinal cord and esophagus no dose differences were detectable. The ROI mapping approach underestimated maximum doses for spinal cord and lung by 0.9% and 0.5%, respectively, while maximum esophagus and mean lung dose were overestimated by 0.1% for both. For the WAB method maximum spinal cord and lung dose were underestimated by 1.1% and 1.3%, respectively. However, maximum esophagus dose was overestimated by 0.2%, compared to the CCP technique, while for mean lung dose no dose difference was detectable. In *figure* 8 doses for OARs are shown.

### 5.1.3 Head and Neck cases

In contrast to prostate and lung cases, head and neck plans include two PTVs, which are planned with differenct dose levels of 50Gy and 60Gy, respectively. As already mentioned before, this is achieved by using a SIB method. PTV coverage for both PTVs is presented in *figure* 36.

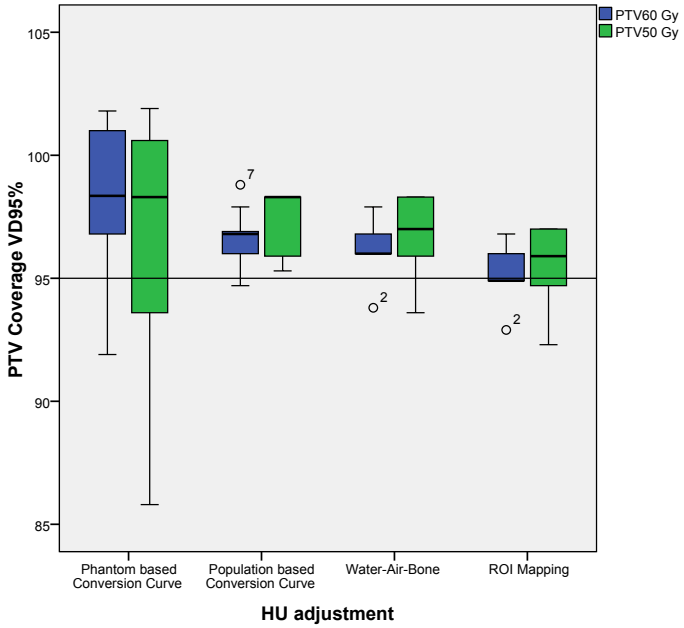


Figure 36: H& N PTV coverage for 95% of prescribed dose for each PTV. PTV 60Gy is plotted in blue, PTV 50Gy is plotted in green.

The phantom-based conversion curve method showed highest range for both, 25% - 75% percentile and range of values. However, median PTV coverage for

both PTVs was higher than for every other method, i.e. it was 98.3% for both PTVs. In general both conversion curve based methods provided higher coverage for nearly every case compared to the WAB and ROI mapping techniques. This is true for PTV 50Gy and PTV 60Gy. Nonetheless, all methods reached on average the 95% coverage objective for both PTVs, except PTV 60Gy for the ROI mapping technique. There PTV coverage was slightly below 95% with 94,9%. For the non conversion curve based methods, case 2 (PTV 60Gy) was an outlier, whereas for the population based conversion curve technique case 7 (PTV 60Gy) was found to be an outliers. The statistical range of the phantom-based conversion curve technique was big enough to include PTV coverage for cases 2 and 7 as well and no outliers were detected.

In *figure* 37 median PTV doses for PTV 50Gy and PTV 60Gy are shown.

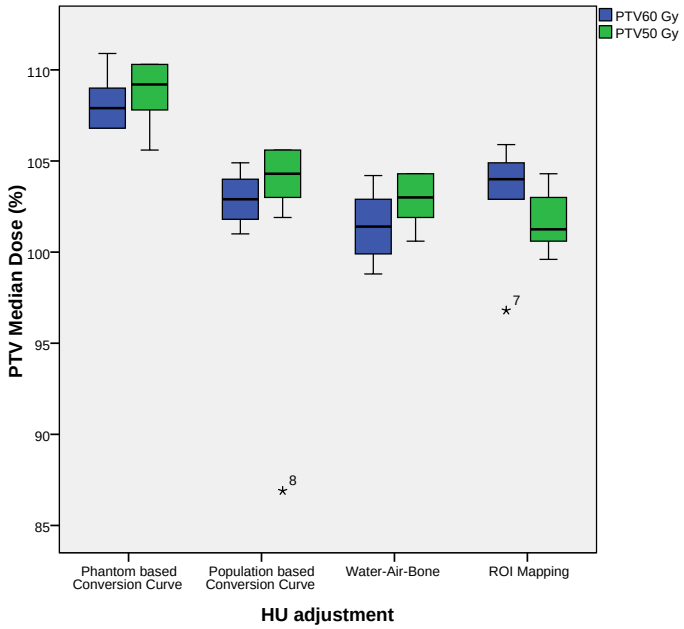


Figure 37: Median PTV doses for head and neck cases. PTV 60Gy is plotted in blue, PTV 50Gy is plotted in green.

Median PTV median dose for the phantom-based conversion curve method showed for both PTVs significantly higher doses than for the CCP, WAB and ROI mapping techniques. Median dose values for PTV 60Gy were 107.9, 102.9, 101.4 and 104 for the CC, CCP, WAB and ROI approaches, respectively. While the phantom-based conversion curve and water-air-bone method provided doses just higher than 100%, the ROI mapping and population-based conversion curve methods provided at least one single case with median doses below 100% of the prescribed dose for both PTVs. Case 7 and 8 were outliers at the CCP and ROI mapping method respectively.

In *table* 9 doses for OARs are presented.

Table 9: Median doses for organs at risk in % of prescribed dose for 3D SBRT lung plans.

| | CC | CCP | WAB | ROI |
|---|---|---|---|---|
| Spinal Cord $D_{Max}$ | 79.6 [81.4±4.8] | 75.2[76.7±4.4] | 73.5 [74.1±2.1] | 73 [73.5±1.9] |
| Brainstem $D_{Max}$ | 75 [72±11.2] | 70.4 [67.8±10.3] | 70 [68±10.2] | 68 [66.2±9.7] |
| Parotid gland $D_{Mean}$ | 43.2 [46.5±11.6] | 41.7 [44.9±10.9] | 41.9 [45.3±10.8] | 41.7 [44.6±10.6] |

For all OARs, the phantom-based conversion curve technique provided highest median doses compared to all other methods. In more detail, for the CC method, maximum spinal cord, maximum brainstem and mean parotid gland dose were overestimated by 4.4%, 4.6% and 1.5%, respectively, compared to the "golden standard", the CCP method. In addition, the CC technique also showed the largest standard deviation of all methods. For maximum spinal cord dose mean and median value as well as the standard deviation were underestimated by the non conversion curve based methods. While the WAB technique underestimated maximum spinal cord and maximum brainstem doses by 1.7% and 0.3%, mean doses for parotid gland were underestimated by 0.2%. The ROI mapping method underestimated both, maximum spinal cord and maximum brainstem dose by 2.2% and 2.4%, respectively. However, for the mean dose of the parotid gland no difference to the CCP method was detectable.

## 5.2 $\gamma$- Evaluation

In this section gamma evaluation results are presented, comparing different methods for adaptive treatment planning. Due to physical factors like different field of view (FOV), scattering and artifacts images of the same patient may differ enormously. A comparison of dose exports of CT images with dose exports of CBCT images for different cases showed that the $\gamma$-index was mainly influenced by the geometric differences. As already mentioned in section 4.3.2, the $\gamma$-angle plays an important role in evaluating the results of $\gamma$-evaluation: if the $\gamma$-angle is between 0 and $\pi/4$ the $\gamma$-index is dominated by the dose difference, if between $\pi/4$ and $\pi/2$ the $\gamma$-index is dominated by the DTA.
In literature the population- based conversion curve method has been marked as reliable and providing accurate enough results [26]. Therefore, $\gamma$-evaluation was performed by comparing dose distributions of the water-air-bone and ROI mapping approaches to dose distributions of the population-based conversion curve method. The phantom-based conversion curve approach is not used because it showed the worst results of all methods in the DVH- comparison section. Due to the usage of CBCT data on both sides of the test, geometric uncertainties between CT and CBCT are not taken into account. The $\gamma$-index is therefore mainly influenced by dose differences.
$\gamma$-evaluation was performed using "DosVer" software, written by Markus Stock, Department of Radiotherapy at the MUW / AKH Vienna, Austria. For all cases 3mm distance to agreement (DTA) and 3% dose difference as $\gamma$ criteria were used. To evaluate $\gamma$- values more precisely, regions of interest (ROIs) were defined, excluding manipulating air pixels. Therefore only values within that region were analyzed.

To make reading easier the following nomenclature is used in the next section: $x,y$ and $z$ direction describe transversal, sagittal and vertical movement, respectively.

### 5.2.1 Prostate cases

**$\gamma$- evaluation of 4Fbox plans** For prostate cases dose distributions in transversal plane were exported at isocenter and in planes 16mm above and 16mm below ($z$-plane). The size of the exported image was reduced to isocenter position $\pm$ 150 pixel in $x$ direction and $\pm$ 100 pixel in $y$ direction, due to a lack of information outside this region. The Region of interest was placed symmetrical around the isocenter, in rectangular shape. To exclude air pixels effectively, the size of the plane was reduced by 30 pixel on each side, resulting in a ROI size of $\pm$ 120 pixel in $x$ direction and $\pm$ 70 pixel in $y$ direction. In *figure* 38 an average prostate case is shown.

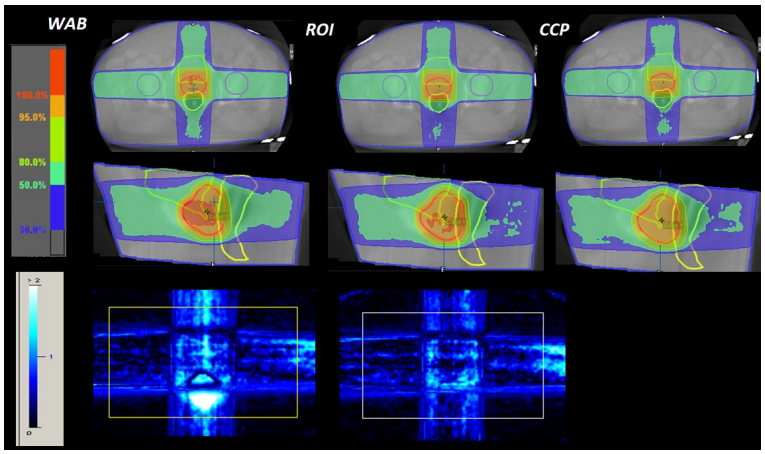


Figure 38: Comparison of dose distribution for transversal and sagittal planes for an average prostate case. In the third row $\gamma$-values are shown, were ROI is marked yellow.

In the first row transversal slices, in the second row sagittal slices are shown for the WAB, ROI and CCP approaches. Additionally colored dose distributions, PTV and OARs outlines are shown as well. A slight overestimation of the PTV dose for the WAB approach is recognizable, which is a consequence of changing the density of rectal balloon to air equivalent. In the third row, results of $\gamma$-evaluation are shown. The images show corresponding $\gamma$-values for each pixel of the image, coded by color. The brighter the color, the higher the $\gamma$- value, namely dark blue for 0 and white for 2. Additionally the region of interest is marked yellow, representing the analyzed area of the slice.
After performing $\gamma$- evaluation itself, maximum and mean $\gamma$-value in ROI and percentage of $\gamma$-values higher than 1 have been analyzed.
In *figure* 39 the worst of all 10 4Fbox prostate cases is presented.
Obviously there were big differences in dose distribution especially between the population-based conversion curve and non conversion curve based methods. In the transversal plane in anterior-posterior direction strong inhomogeneities are

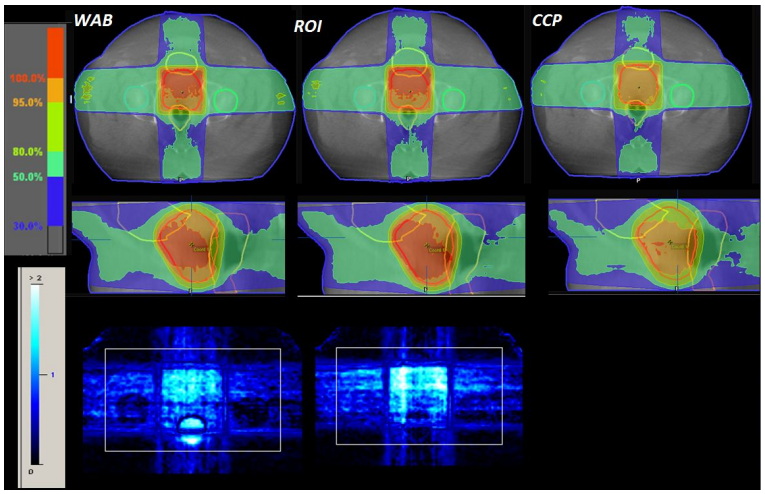


Figure 39: Comparison of dose distribution for transversal and sagittal planes for a bad case prostate case (7) . Due to high BMI of patient and limited size of FOV, CBCT images are cropped compared to planning CT images. In the third row $\gamma$-values are shown, were ROI is marked yellow.

present. Additionally minor inhomogeneities are visible in the sagittal plane too. In contrast to another case, i.e. case 7, it shows extremely poor CBCT image quality, including very strong ring artifacts. However, differences between the water-air-bone and ROI mapping approaches were not significantly high. Therefore the non-conversion curve based methods like the water-air-bone and ROI mapping approaches seem to be more robust to poor image quality compared to the conversion curve based techniques.
In *table* 10 mean values for 10 prostate cases are presented.

Table 10: $\gamma$-values for prostate cases using 4Fbox plans

| | Water-Air-Bone | ROI mapping |
|---|---|---|
| $\gamma_{Max}$ | 2.2 | 1.8 |
| $\gamma_{Mean}$ | 0.4 | 0.4 |
| $\gamma > 1$ | 4.9% | 4.7% |

The water-Air-Bone technique shows higher mean values compared to the ROI mapping approach. In more detail, the difference of the maximum $\gamma$- value is 0.6, while the mean $\gamma$- value is identical. The difference in the amount of $\gamma$-values higher than one is negligible with 0.2%.

**$\gamma$- evaluation of IMRT plans** For IMRT plans, export properties and size of ROI are identical to 4FBox plans. In *figure* 40 an average case for IMRT prostate plans is shown.
As already mentioned before, for IMRT prostate plans 7 beams are used instead of four. In *figure* 41 a bad case for IMRT plans is presented.

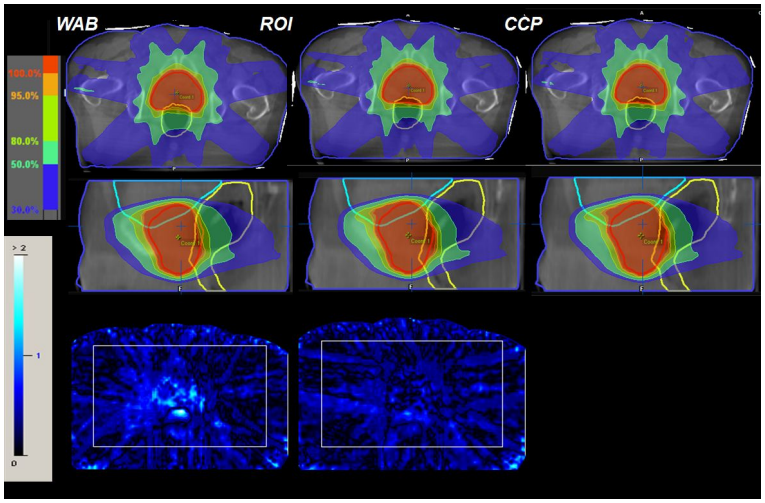


Figure 40: Comparison of dose distribution for transversal and sagittal planes for an average prostate case (3). In the third row $\gamma$-values are shown, were ROI is marked yellow.

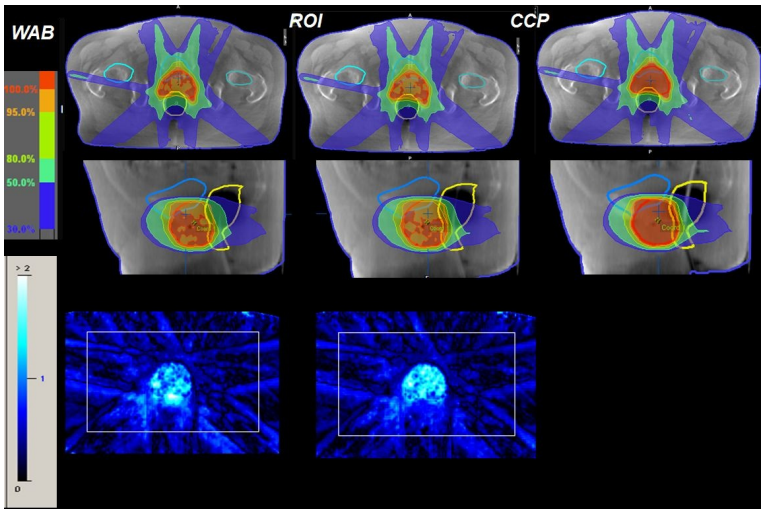


Figure 41: Comparison of dose distribution for transversal and sagittal planes for the worst prostate case (9). In the third row $\gamma$-values are shown, were ROI is marked yellow.

For both non conversion curve- based methods, namely the WAB and ROI mapping approaches, dose distributions were quite identical. However, the population-based conversion curve technique showed significantly higher doses in the PTV. The overestimation of the PTV dose was caused by a higher overall density of patient 9 compared to the other patients. Especially in third row of the figure it is easy to see that the dose differences mainly occur in the PTV.

In *table* 11 mean $\gamma$-values for IMRT prostate plans are presented.

Table 11: $\gamma$-values for prostate cases using IMRT plans

| | Water-Air-Bone | ROI mapping |
|---|---|---|
| $\gamma_{Max}$ | 2.1 | 1.7 |
| $\gamma_{Mean}$ | 0.4 | 0.3 |
| $\gamma$ >1 | 4.5% | 3% |

Due to the higher number of beams used for IMRT treatments, every single value evaluated for $\gamma$- evaluation decreased compared to 4FBox plans. In more detail, maximum $\gamma$- value decreased by 0.1, while the mean $\gamma$- value decreased by 0.06 and 0.1 for the WAB and ROI mapping approaches, respectively. A simple explanation is that both, PTV coverage and OAR sparing increased due to a higher number of beams used, providing a more accurate possibility of superimposition to cover uncertainties. However, the water-air-bone approach showed higher values compared to ROI mapping. Again, mean $\gamma$-value showed negligible differences, while maximum $\gamma$-value differs more strongly by 0.4. Additionally 1.5% more pixels showed $\gamma$-values higher than 1 compared to the ROI mapping technique.

### 5.2.2 Lung cases

For lung cases transversal slices were acquired for dose exports, sized 146 pixel in $x$ and 180 pixel in $y$ direction. However, the resulting area may not be symmetrical around the isocenter. Additionally the distance between two exported slices was reduced from 16mm (for prostate cases) to 8mm in $z$ direction for lung cases. In *figure* 42 transversal dose distribution and distribution of $\gamma$- values is shown for an average lung case.
As already mentioned before, for 3D SBRT plans 9 conformal beams were used. The region of interest was set 20 pixel smaller than the image in $x$ and $y$ direction. In *figure* 43 the worst case of all lung cases is presented.
Especially at low density lung tissue and at bone- lung interfaces dose differences between the CCP method and the non conversion curve based methods are shown. The second row of *figure* 43 shows clearly, that dose differences mainly occur inside the region of interest. Again poor image quality and various artifacts may be the reason for the differences in dose calculation.

In *table* 12 mean values of all lung cases are presented.
Compared to IMRT prostate plans nearly all values presented in *table* 12 increased for both, the WAB and ROI mapping approaches, due to the inability of conformal beams to modulate intensity. While the median *gamma*- value increased by 0.1, the percentage of $\gamma$- values higher than one increased by 1.6% and

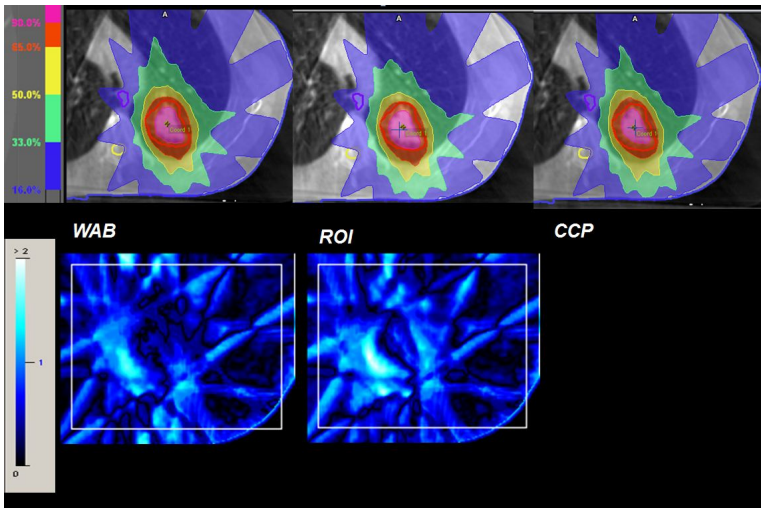


Figure 42: Comparison of dose distributions for transversal planes for an average lung case (7). In the second row $\gamma$-values are shown, were ROI is marked white.

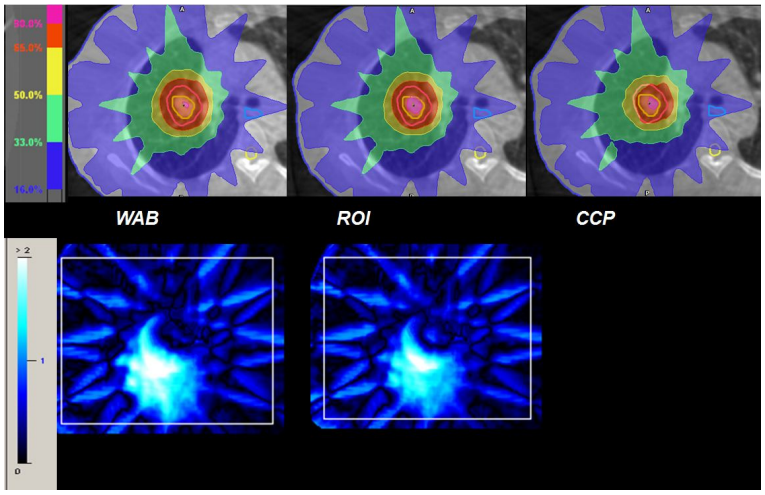


Figure 43: Comparison of transversal dose distributions for the worst lung case (9). Anatomical differences to other lung cases are the reason for the bad dose distribution: i.e. case 9 shows a tumor with diffuse spreads in the low density lung tissue, where dose differences mainly occur. In the second row plotted $\gamma$-values are shown, were the ROI is marked white.

Table 12: $\gamma$-values for lung cases using 3D SBRT plans

| | Water-Air-Bone | ROI mapping |
|---|---|---|
| $\gamma_{Max}$ | 1.8 | 1.6 |
| $\gamma_{Mean}$ | 0.5 | 0.4 |
| $\gamma$ >1 | 6.1% | 5.1% |

2.1% for the WAB and ROI mapping approaches, respectively. Only maximum $\gamma$- values are lower compared to prostate cases. However, differences between the water-air-bone and ROI mapping techniques are smaller than for prostate cases. The water-air-bone method showed nearly equal results compared to the ROI mapping technique.

### 5.2.3 Head and neck cases

For head and neck cases complete transversal slices were exported, i.e. no changes in size were done. Slices were exported at the position of the isocenter and $\pm$ 16mm in $z$ direction. No fixed sizes were used, but it was fitted according to the anatomical situation of each case. In more detail, the ROI was selected to include the spinal cord and tumor as good as possible, but to spare air and the head support pillow efficiently. In *figure* 44 dose distributions for transversal and sagittal slices and distribution of $\gamma$ values are presented.

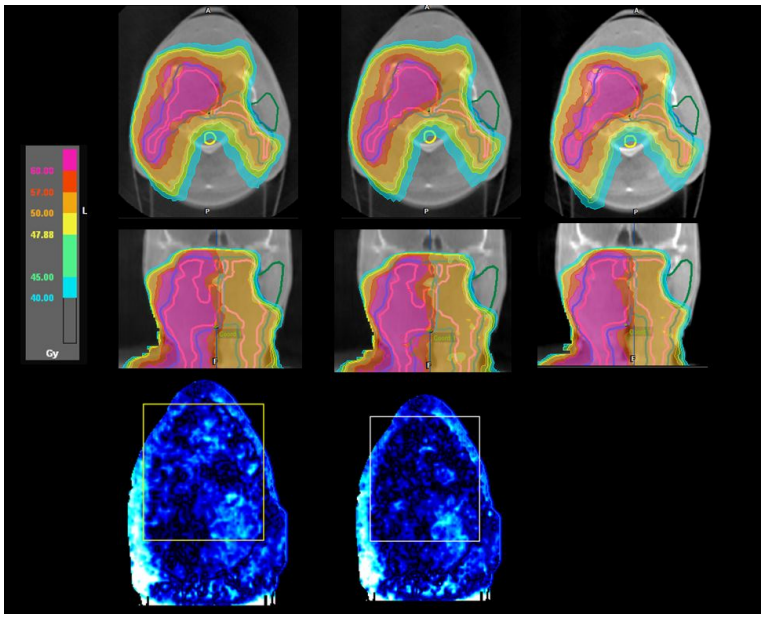


Figure 44: Comparison of dose distributions for transversal and sagittal planes for an average H & N case. In the third row $\gamma$-values are shown, were the ROI is marked yellow. Obviously dose deviations occurred mainly at the location of the mask and patient surface.

For H & N cases no bad cases or outliers were found. Mean $\gamma$- values for H & N cases are presented in *table* 13.
For head and neck cases the water-air-bone technique showed better results than the ROI mapping approach. The maximum $\gamma$- value for the WAB approach was 0.1 lower compared to the ROI mapping technique. The difference for mean $\gamma$-value was 0.1 too. Only for the amount of $\gamma$- values higher than one, higher differences occurred, i.e. 1.2%. Although differences between both methods were not significantly, the WAB method is preferable for H & N cases, due to slightly better results.

Table 13: $\gamma$-values for H & N cases using IMRT plans

| | Water-Air-Bone | ROI mapping |
|---|---|---|
| $\gamma_{Max}$ | 1.9 | 2 |
| $\gamma_{Mean}$ | 0.4 | 0.5 |
| $\gamma$ >1 | 5.1% | 6.3% |

## 5.3 CBCT / CT comparison

The water-air-bone and ROI mapping approaches are compared to CT plans in a next step, based on the promising results for CBCT- based dose recalculation reported in previous sections. Evaluation will be performed by DVH-evaluation as well as discussion of single cases, if necessary.

### 5.3.1 Prostate cases

PTV coverage for four field box planned prostate cases is presented in *figure* 45.

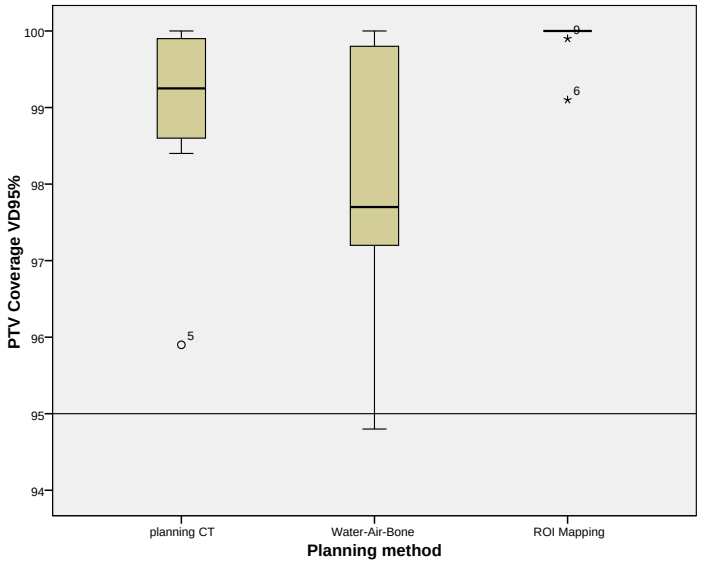


Figure 45: PTV coverage for 4Fbox prostate cases

For all approaches PTV coverage was distinctly higher than required, i.e. 95%. Case 6 showed, for the water-air-bone approach, a coverage slightly below 95% (94.8%), although coverage for planning CT and ROI mapping technique was 99.1%. However, the WAB approaches showed a wide statistical range caused by a broad variation of values. Therefore case 6 is no outlier, which means that it is numerically not very different from the rest of the data. In contrast to that case 5 is an outlier for the CT based plan, showing a PTV coverage of 95,9%. The water-air-bone and ROI mapping techniques overestimated PTV coverage by 1.3% and 4.1%, respectively. The ROI mapping method showed 100% PTV coverage for all cases, except case 6 (99,1%) and 9 (99,9%), which

were therefore detected as outliers. The ROI mapping approach overestimated PTV coverage, showing a mean value of 1%, whereas the WAB- method tended to underestimate PTV coverage in mean by 1%.
In *figure* 46 median PTV doses for the 4Fbox prostate cases are shown.

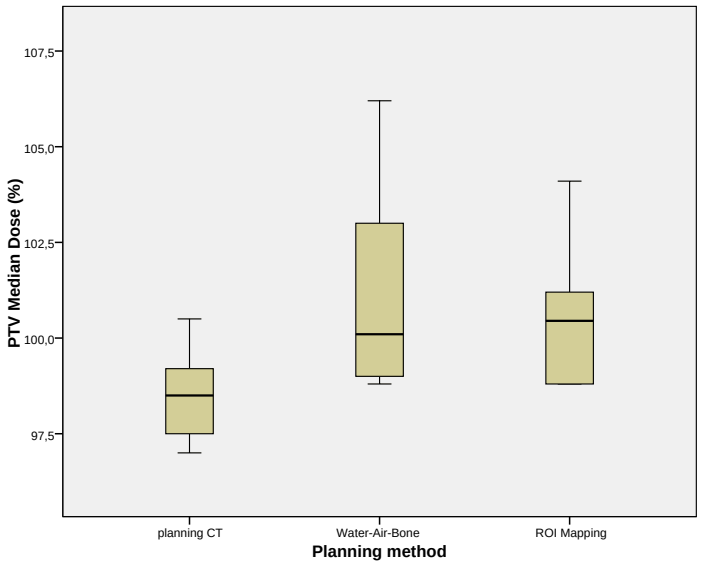


Figure 46: Median PTV doses in percent of prescribed dose for prostate cases using 4FBox planning technique.

For median PTV doses both non conversion curve based methods showed a slight overestimation for every single case compared to original CT plans. In more detail, the water-air-bone technique overestimated median PTV doses by a mean value of 2.5% and the ROI mapping approach by a mean value of 2% of the prescribed dose. No extreme outliers were detected.
In *table* 14 median differences for organs at risk in percent of prescribed dose are shown.

Table 14: Median differences to planning CT for organs at risk doses in % of the prescribed dose for 4Fbox prostate plans.

| | WAB | ROI |
|---|---|---|
| Rectum $D_{Max}$ | 2 [2.4±2.9] | 1.8 [2±1.8] |
| Rectum $D_{Mean}$ | 2.9 [3.7±3.5] | 3.8 [4.3±3.7] |
| Bladder $D_{Max}$ | 2.2 [2.5±2.9] | 0.2 [0.5±2] |
| Bladder $D_{Mean}$ | 5.4 [7.2±10.1] | 3.3 [6.5±10] |

For all organ at risks both methods overestimated doses. The maximum rectum dose was overestimated by the on average by 2% and 1.8% of the prescribed dose by the WAB and ROI mapping approaches, respectively. Furthermore, the WAB approach overestimated maximum and mean bladder doses stronger than the ROI mapping approach compared to original CT. Only for mean rectum

doses the WAB technique showed smaller median values compared to the ROI mapping technique. Additionally, the ROI mapping method showed smaller standard deviations compared to the WAB method.
For IMRT based prostate plans PTV coverage is presented in *figure* 47.

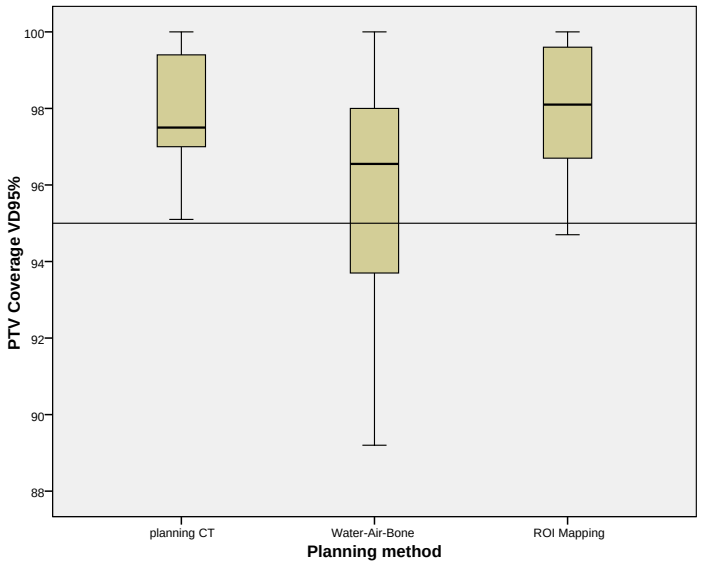


Figure 47: PTV coverage for IMRT planned prostate cases

For planning CT and both adjustment methods the median PTV coverage was above 95%. For planning CT all cases showed a PTV coverage higher than 95%, although case 6 and 9 barely fulfilled the criterion showing a coverage of 95.1%. However, the water-air-bone method has four cases (6,8,9 and 10) with a PTV coverage smaller than 95%, showing values of 89.2%, 94.9%, 93.4% and 93.7%, respectively. The ROI mapping technique showed just one single case with PTV coverage slightly below 95%, i.e. case 9 with 94.7%. Nonetheless, the water-air-bone method showed the highest statistical range compared to planning CT and the ROI mapping technique. This is caused by a higher amount of patient to patient differences. While the ROI mapping approach showed PTV coverages for all cases in the range between 94.7% and 100%, the water-air-bone technique showed PTV coverages between 93.4% and 100%.
In contrast to previous sections, where all compared planning techniques were based on CBCT images, now plans based on planning CT and CBCT are compared. Therefore anatomical changes, like physiological organ movement, have to be considered as well and may be an additional reason of dose differences. Due to violation of IMRT plan requirements concerning PTV coverage using the WAB and ROI mapping methods, re-planning may be necessary. However, due the fact that also planning CT based plans show quite low coverage it is not absolutely necessary. In general the WAB method underestimated PTV coverage by a mean value of 1.88%, whereas ROI mapping technique overestimated PTV coverage by a mean value of 0.25%.
In *figure* 48 median PTV doses are presented.

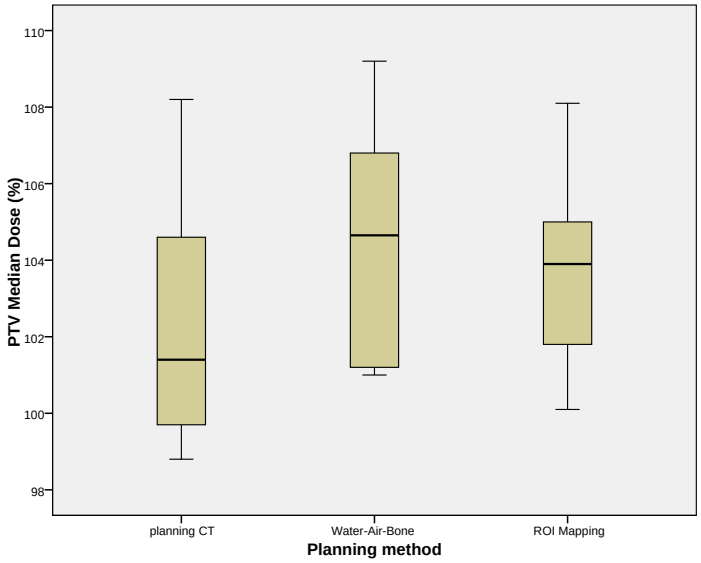


Figure 48: Median PTV dose for prostate cases using IMRT based planning technique. Dose is given in % of prescribed dose.

For both techniques, WAB and ROI mapping, the median PTV dose was overestimated compared to planning CT by 2.2% and 1.5%, respectively. Even median PTV doses for every single case were overestimated by both techniques compared to planning CT, except case 1 and 10 at the ROI mapping approach. However, both approaches showed very constant and predictable results.
In *table* 15 dose differences between planning CT and CBCT based plans are shown.

Table 15: Median differences to planning CT for organs at risk doses in % of prescribed dose for IMRT prostate plans. Entries consist of median value in front, mean value and standard deviation in brackets (Median [Mean ± SD])

| | WAB | ROI |
|---|---|---|
| Rectum $D_{Max}$ | 0.4 [0.7±2.1] | 0.7 [1.1±1.4] |
| Rectum $D_{Mean}$ | 2.2 [3.1±2.8] | 1.9 [2.7±3.5] |
| Bladder $D_{Max}$ | 0.7[1.5±2.5] | 0.3 [0.6±2.5] |
| Bladder $D_{Mean}$ | 3 [6.4±10.8] | 2.9 [6.4±10.6] |

Both, the water-air-bone and ROI mapping approaches showed extremely good agreement with planning CT based doses. Median dose differences were 0.4% and 0.7% for maximum rectum dose and 0.7% and 0.3% for maximum bladder dose. For mean doses differences compared to planning CT were $\leq$ 3% of the prescribed dose for both techniques. In contrast to the 4Fbox based plans, OAR doses for IMRT plans showed even better agreement with CT.

### 5.3.2 Lung cases

In *figure* 49 PTV coverage for 3D SBRT planned lung cases is shown.

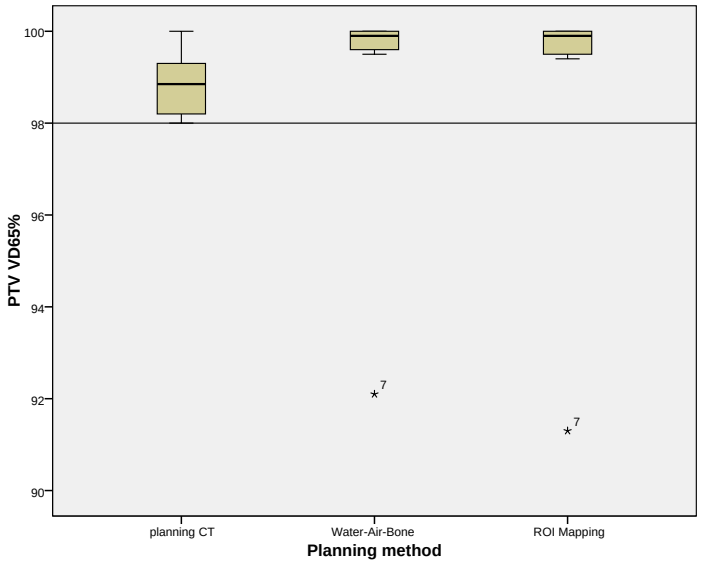


Figure 49: PTV coverage for 3D SBRT planned lung cases.

All cases, except case 7 for the WAB and ROI mapping techniques, showed high PTV coverage above 98%. However, in planning CT based plans all cases showed a coverage higher than 98%. Therefore it is interesting that patient 7 showed such a strongly decreased PTV coverage. Furthermore, both non conversion curve based methods overestimated doses compared to the planning CT based dose distribution (by 0.2% and 0.1%, respectively). Only case 7 showed significantly lower doses (98% coverage in planning CT, 92.1% and 91.3% for the WAB and ROI mapping approaches, respectively). The first reason for the bad PTV coverage is that the tumor tissue of case 7 is very diffuse. Additionally, due to longer acquisition times of the CBCT, breathing led to a larger and blurred projection of the tumor in the CBCT images. Furthermore tumors in general appeared "softer" and less dense in CT compared to CBCT, due to imaging properties. To increase the PTV coverage of case 7 either re-planning or re-scanning would be necessary in clinical routine.
In *figure* 50 median PTV doses are presented.
Both non conversion curve based methods overestimated the median PTV dose compared to the planning CT. The median difference of median PTV doses for the water-air-bone method compared to the planning CT was 5.6% For the ROI mapping technique median PTV dose was overestimated by 4.6% of the prescribed dose. For both methods no outliers were found.
Dose differences for OARs compared to planning CT are shown in *table* 16.
Doses for organs at risk, including maximum dose for spinal cord, maximum dose for esophagus and maximum dose for Lung were slightly underestimated by both methods, water-air-bone and ROI mapping. Only mean lung doses were

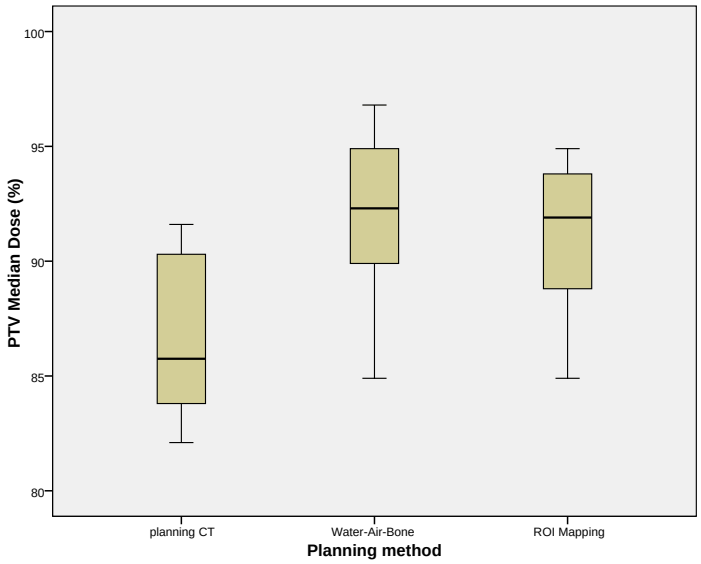


Figure 50: Median PTV doses for 3D SBRT lung plans.

Table 16: Median differences to planning CT for organs at risk doses in % of prescribed dose for 3D SBRT lung plans.

| | WAB | ROI |
|---|---|---|
| Spinal cord $D_{Max}$ | -1 [-0.5±1.4] | -0.6 [-0.3±1.3] |
| Esophagus $D_{Max}$ | -0.5 [-0.3±1] | -0.4 [-0.3±1] |
| Lung $D_{Max}$ | -1.2[-0.8±2.3] | -0.7 [-1.1±1.9] |
| Lung $D_{Mean}$ | 0.2 [0.5±0.7] | 0.3 [0.6±0.7] |

slightly overestimated compared to the planning CT, i.e. by 0.2% and 0.3% for the WAB and ROI mapping techniques, respectively. However, median dose differences to planning CT were lower than 1.3% and therefore negligible.

### 5.3.3 Head and neck cases

For H & N cases PTV coverage for PTV 60Gy and PTV 50Gy are shown in *figure* 51.

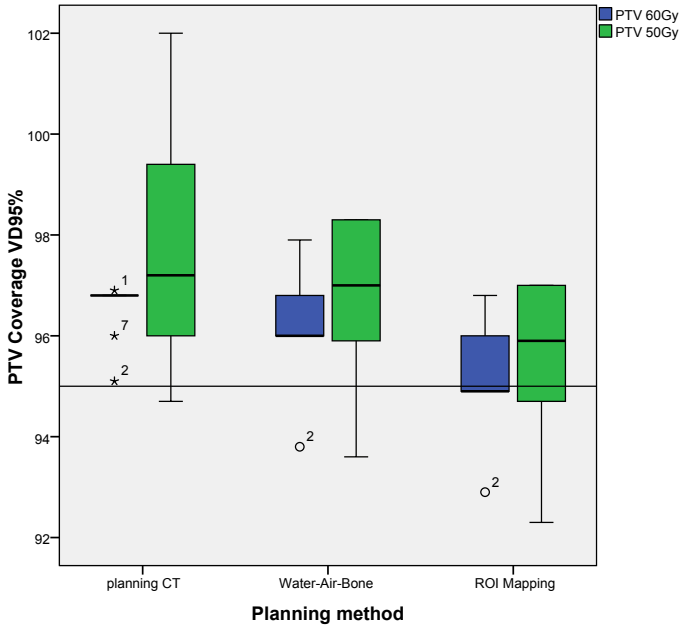


Figure 51: PTV coverage for head and neck cases. PTV 60Gy is plotted in blue, PTV 50Gy is plotted in green.

PTV coverage for PTV 60Gy and PTV 50Gy was slightly underestimated by both non conversion curve based methods. While the water-air-bone technique underestimated PTV 60Gy coverage by 0.3%, the ROI mapping approach underestimated it by 1.4%. PTV coverage for PTV 50Gy was underestimated by 0.6% and 1.9% for the WAB and ROI mapping approaches, respectively. Planning CT based dose distribution provided PTV 60Gy coverage higher than 95% for every single case. The WAB and ROI mapping techniques showed coverage with 93.8% and 92.9% for case two, while the planning CT based plan showed a PTV coverage of 95.1%. The decrease of PTV coverage was caused by anatomical changes in CBCT images compared to planning CT images. Additionally case 1 and 7 were marked as outliers, although both cases showed a PTV coverage above 95%, due to a very small 25% to 75% percentile interval. However, PTV 50 Gy coverage for case 2 was above 95%. Nonetheless, for PTV 50Gy planning CT based dose distribution showed PTV coverage below 95% for case 9 (94.7%). Following the underestimating trend of the WAB and ROI mapping

methods, case 9 showed PTV coverage below 95% too.
In *figure* 52 median PTV doses for PTV 60Gy and PTV 50Gy are presented.

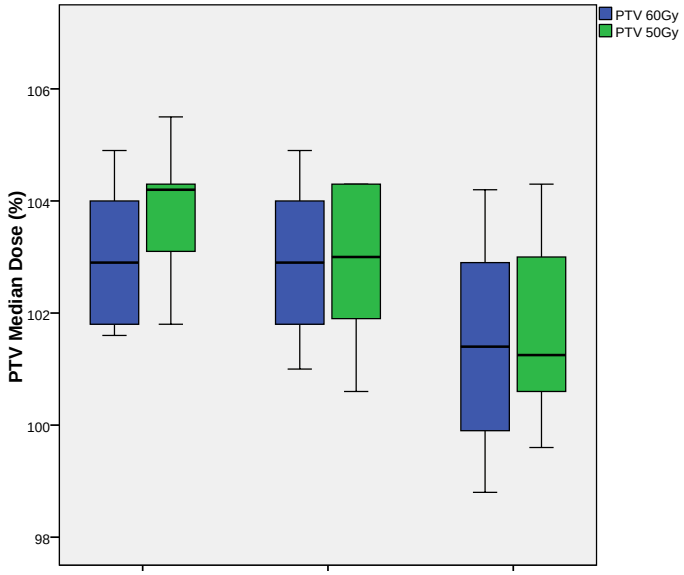


Figure 52: Median PTV doses for head and neck cases. PTV 60Gy is plotted in blue, PTV 50Gy is plotted in green.

Median PTV doses showed comparable results for both PTVs and both techniques, water-air-bone and ROI mapping. The median PTV 60Gy dose was underestimated by the WAB and ROI mapping techniques by an average value of 0.3% and 1.9%, respectively. Quite similar results were provided for the PTV coverage of PTV 50Gy, where the WAB technique underestimated by an average value of 0.8%. The ROI mapping approach underestimated by an average value of 2.1%. Due to the fact that case 4 was marked as an outlier for all planning methods, including planning CT, no need for re- planning is given.
In *table* 17 median and mean doses as well as standard deviations for head and neck cases are presented.

Table 17: Median dose differences to planning CT based plans for organs at risk for IMRT head and neck plans. Doses are given in % of the prescribed dose.

| | WAB | ROI |
|---|---|---|
| Spinal cord $D_{Max}$ | -1.4 [-1.2±2.3] | -2.4 [-1.7±2.2] |
| Brainstem $D_{Max}$ | -0.3 [0±1.8] | -1.6 [-1.8±1.5] |
| Parotid gland $D_{Mean}$ | 0.1[-0.1±1.4] | -0.5 [-0.8±1.4] |

Median dose differences for maximum dose of spinal cord and brainstem were underestimated by both methods. While the WAB approach underestimated maximum doses for the spinal cord on average by 1.4%, the ROI mapping

technique underestimated it by 2.4%. Median dose differences for maximum brainstem dose was underestimated by 0.3% and is therefore negligible. The ROI mapping method underestimated maximum doses for brainstem by 1.6%. Both methods showed very small dose differences for the median parotid gland dose, namely -0.1% for the WAB and 0.5% for the ROI mapping technique.

# 6 Conclusion and Outlook

Both, the ROI mapping and WAB methods provide alternative approaches to the population- based conversion curves for CBCT dose calculation. Differences below 3% for PTVs and OARs compared to planning CT based dose distributions demonstrate reasonable accuracy of the dose calculation for both methods together with required sensitivity to detect anatomic changes in the IGART process. After analyzing over 30 cases re-planning was necessary only for one case of each group (for prostate case 6, for lung case 7 and for H & N case 7). While the WAB and ROI mapping methods tended to overestimate doses for prostate and lung cases, both methods slightly underestimated doses for head and neck cases. The WAB technique is associated with smallest workload in the routine, whereas the ROI mapping method requires knowledge of patient- specific electronic density (ED) information. In more detail, applying the WAB correction method on a CBCT image set takes less than a minute in clinical routine, due to the fact that density information of only three different structures has to be replaced with standard values. However, applying the ROI mapping technique is much more time consuming, due to the fact that average HUs for all OARs have to be determined in the planning CT image set and applied to the CBCT image set. Additionally it has to be done for each patient individually. It will take up to 10 minutes for each patient, according to the level of experience in the TPS used. Therefore the water-air-bone approach is an promising and reliable method for adaptive radiotherapy, if workload and dose accuracy are considered.

In future research the applicability for other anatomic sites, besides prostate, lung and head and neck tumors, could be tested. Due to physiological anatomical movement diseases like gynecology and rectal cancer would be an obvious choice. Additionally refined HU values for various applications could be investigated to improve the accuracy of the WAB approach. Furthermore, a validation of calculated dose values could be done by irradiating various phantoms in the LINAC.
Another step towards higher efficiency would be to develop a software tool for various treatment planning systems which automatically applies the WAB approach on a CBCT image set. Due to performance issues some kind of "plugin" for the TPS would be preferable, if some kind of software development kit is available for the desired TPS. However, a stand alone tool in an open source software environment, like "Octave" [7], may provides a cheap and effective alternative. Another major advantage would be the possibility of an universal usability with various commercial TPS.

[7] GNU Octave, http://www.gnu.org/software/octave/

# A Matlab Code

## A.1 "CT-Files" - Conversion

```
for j=1:1:10
    p_num = num2str(j);
    abstand = '16';

dateinamenCT1 = ['P',p_num,'CTiso'];
dateinamenCT2 = ['P',p_num,'CT','+', abstand, 'mm'];
dateinamenCT3 = ['P',p_num,'CT','-', abstand, 'mm'];

for i=1:1:3
    switch i
        case 1
            name = dateinamenCT1;
        case 2
            name = dateinamenCT2;
        otherwise
            name = dateinamenCT3;
    end

    text = textread(name,'%s', 'delimiter', '\t','whitespace', '');
   %text = textread('P3CTiso', '%s', 'delimiter', '\t','whitespace', '');
    rows = str2double(text(32,1));
    columns = str2double(text(34,1));
    starting_point = 37; %in dieser Zeile beginnt der Datensatz (die ersten Zeile ist
    %die Position in mm)!
    dateinamenCT_out = strcat(name,'out.csv');
    fid = fopen(dateinamenCT_out, 'w');
    %fid = fopen('CTout.csv', 'w');
    fprintf(fid, 'AP \\ LR');
    for i= starting_point+1:1:length(text)
        if(i<=(starting_point + (columns))) %Erste Zeile sind
    %Längenangaben die von mm in CM umgerechnet werden
            fprintf(fid,';%f',(str2double(text(i,1))/10));
        elseif(mod((i-(starting_point)),(columns+1)) == 0)    %Index - Headerlänge Mod
    %colums+2 == Angabe in mm --> Muss in CM umgerechnet werden
            fprintf(fid,'\n %f',(str2double(text(i,1))/10));
        else
            fprintf(fid,';%f',str2double(text(i,1)));
        end
    end
    fclose(fid);
end
end
```

## A.2 "Film-files" - Conversion

```
for j=1:1:10
    p_num = num2str(j);
    abstand = '16';

dateinamenCBCT1 = ['P',p_num,'CBCT1iso'];
dateinamenCBCT2 = ['P',p_num,'CBCT1','+', abstand, 'mm'];
dateinamenCBCT3 = ['P',p_num,'CBCT1','-', abstand, 'mm'];
dateinamenCBCT4 = ['P',p_num,'CBCT2iso'];
dateinamenCBCT5 = ['P',p_num,'CBCT2','+', abstand, 'mm'];
dateinamenCBCT6 = ['P',p_num,'CBCT2','-', abstand, 'mm'];
dateinamenCBCT7 = ['P',p_num,'CBCT3iso'];
dateinamenCBCT8 = ['P',p_num,'CBCT3','+', abstand, 'mm'];
dateinamenCBCT9 = ['P',p_num,'CBCT3','-', abstand, 'mm'];

for i=1:1:9
    switch i
        case 1
            name = dateinamenCBCT1;
        case 2
            name = dateinamenCBCT2;
        case 3
            name = dateinamenCBCT3;
        case 4
            name = dateinamenCBCT4;
        case 5
            name = dateinamenCBCT5;
        case 6
            name = dateinamenCBCT6;
        case 7
            name = dateinamenCBCT7;
        case 8
            name = dateinamenCBCT8;
        otherwise
            name = dateinamenCBCT9;
    end


text = textread(name, '%s', 'delimiter', '\t','whitespace', '');
rows = str2double(text(34,1));
columns = str2double(text(36,1));
starting_point = 39; %in dieser Zeile beginnt der Datensatz
dateinamenCBCT_out = strcat(name,'out.txt');
fid = fopen(dateinamenCBCT_out, 'w');
for i= starting_point+rows:1:length(text)
    if(i<=(starting_point + (columns)))
        ;
    elseif(mod((i-(starting_point)),(columns+1)) == 0) %Index - Headerlänge
    %Mod colums+2 == Angabe in mm --> Muss in CM umgerechnet werden
```

```
        if i > (starting_point+columns+1)
            fprintf(fid,'\n');
        end
    else
        fprintf(fid,'   %e',str2double(text(i,1)));
    end
end
fclose(fid);
end
end
```

# References

[1] S. A. Bhide and C. M. Nutting.
Recent advances in radiotherapy.
*BMC Med*, 8:25, 2010.

[2] Thomas Bortfeld, Rupert Schmidt-Ullrich, Wilfried De Neve, and David E.Wazer.
*Image-Guided IMRT*.
Springer, 2006.

[3] Thomas Bortfeld and Steve Webb.
Single-arc imrt?
*Phys Med Biol*, 54(1):N9–20, Jan 2009.

[4] C. S. Chui, M. F. Chan, E. Yorke, S. Spirou, and C. C. Ling.
Delivery of intensity-modulated radiation therapy with a conventional multileaf collimator: comparison of dynamic and segmental methods.
*Med Phys*, 28(12):2441–2449, Dec 2001.

[5] Olaf Dössel.
*Bildgebende Verfahren in der Medizin: Von der Technik zur medizinischen Anwendung*.
Springer, 1 edition, 2008.

[6] Irina Fotina.
Pre-clinical verification of the treatment planning system with monte-carlo dose calculation and biological optimization.
Master's thesis, Division of Medical Radiation Physics, Department of Radiotherapy, Medical University of Vienna, 2008.

[7] Johannes Hopfgartner.
First steps of implementation of image guided adaptive radiation therapy.
Master's thesis, Division of Medical Radiation Physics, Department of Radiotherapy, Medical University of Vienna, 2009.

[8] Hitoshi Ikushima.
Radiation therapy: state of the art and the future.
*J Med Invest*, 57(1-2):1–11, Feb 2010.

[9] J. A. Purdy R. Timmerman John L. Meyer, B. D. Kavanagh.
*Frontiers of Radiation Therapy and Oncology: IMRT, IGRT, SBRT - Advances in the Treatment Planning and Delivery of Radiotherapy*.
Karger, 2007.

[10] W. Kilby, J. R. Dooley, G. Kuduvalli, S. Sayeh, and C. R. Maurer.
The cyberknife robotic radiosurgery system in 2010.
*Technol Cancer Res Treat*, 9(5):433–452, Oct 2010.

[11] Stine Korreman, Coen Rasch, Helen McNair, Dirk Verellen, Uwe Oelfke, Philippe Maingon, Ben Mijnheer, and Vincent Khoo.
The european society of therapeutic radiology and oncology-european institute of radiotherapy (estro-eir) report on 3d ct-based in-room image guidance systems: a practical and technical review and guide.
*Radiother Oncol*, 94(2):129–144, Feb 2010.

[12] Gopalakrishna Kurup.

Cyberknife: A new paradigm in radiotherapy.
*J Med Phys*, 35(2):63–64, Apr 2010.

[13] Seymour H. Levitt, James A. Purdy, Carlos A. Perez, Srinivasan Vijayakumar, Luther W. Brady, Hans-Peter Heilmann, Michael Molls, and Carsten Nieder.
*Technical Basis of Radiation Therapy: Practical Clinical Applications.*
Springer, 2006.

[14] Taoran Li, Xiaofeng Zhu, Danthai Thongphiew, W. Robert Lee, Zeljko Vujaskovic, Qiuwen Wu, Fang-Fang Yin, and Q. Jackie Wu.
On-line adaptive radiation therapy: feasibility and clinical study.
*J Oncol*, 2010:407236, 2010.

[15] C. Clifton Ling, Ellen Yorke, and Zvi Fuks.
From imrt to igrt: frontierland or neverland?
*Radiother Oncol*, 78(2):119–122, Feb 2006.

[16] D. A. Low, W. B. Harms, S. Mutic, and J. A. Purdy.
A technique for the quantitative evaluation of dose distributions.
*Med Phys*, 25(5):656–661, May 1998.

[17] John L. Meyer.
*Frontiers of Radiation Therapy and Oncology: IMRT, IGRT, SBRT - Advances in the Treatment Planning and Delivery of Radiotherapy*, volume 40.
Karger, 2007.

[18] A. C. Miracle and S. K. Mukherji.
Conebeam ct of the head and neck, part 1: physical principles.
*AJNR Am J Neuroradiol*, 30(6):1088–1095, Jun 2009.

[19] M. A. Mosleh-Shirazi, W. Swindell, and P. M. Evans.
Optimization of the scintillation detector in a combined 3d megavoltage ct scanner and portal imager.
*Med Phys*, 25(10):1880–1890, Oct 1998.

[20] Arno J. Mundt and John C. Roeske.
*Intensity Modulated Radiation Therapy: A Clinical Perspective.*
PMPH USA, 2005.

[21] Mike Oliver, Will Ansbacher, and Wayne A Beckham.
Comparing planning time, delivery time and plan quality for imrt, rapidarc and tomotherapy.
*J Appl Clin Med Phys*, 10(4):3068, 2009.

[22] Karl Otto.
Volumetric modulated arc therapy: Imrt in a single gantry arc.
*Med Phys*, 35(1):310–317, Jan 2008.

[23] Julian R Perks, Jöerg Lehmann, Allen M Chen, Claus C Yang, Robin L Stern, and James A Purdy.
Comparison of peripheral dose from image-guided radiation therapy (igrt) using kv cone beam ct to intensity-modulated radiation therapy (imrt).
*Radiother Oncol*, 89(3):304–310, Dec 2008.

[24] E. B. Podgorsak, editor.
*Radiation Oncology Physics: a handbook for teachers and students.*

IAEA Vienna, 2005.

[25] Jean Pouliot, Ali Bani-Hashemi, Josephine Chen, Michelle Svatos, Farhad Ghelmansarai, Matthias Mitschke, Michele Aubin, Ping Xia, Olivier Morin, Kara Bucci, Mack Roach, Paco Hernandez, Zirao Zheng, Dimitre Hristov, and Lynn Verhey.
Low-dose megavoltage cone-beam ct for radiation therapy.
*Int J Radiat Oncol Biol Phys*, 61(2):552–560, Feb 2005.

[26] Anne Richter, Qiaoqiao Hu, Doreen Steglich, Kurt Baier, Jürgen Wilbert, Matthias Guckenberger, and Michael Flentje.
Investigation of the usability of conebeam ct data sets for dose calculation.
*Radiat Oncol*, 3:42, 2008.

[27] W. Schlegel, T. Bortfeld, and A.-L. Grosu.
*New Technologies in Radiation Oncology.*
Springer, 2006.

[28] Derek Schulze, Jian Liang, Di Yan, and Tiezhi Zhang.
Comparison of various online igrt strategies: The benefits of online treatment plan re-optimization.
*Radiother Oncol*, 90(3):367–376, Mar 2009.

[29] David L Schwartz and Lei Dong.
Adaptive radiation therapy for head and neck cancer-can an old goal evolve into a new standard?
*J Oncol*, 2011, 2011.

[30] S. S. Sivakumar, K. Krishnamurthy, C. A. Davis, R. Ravichandran, S. Kannadhasan, J. P. Biunkumar, and Kamal El Ghamrawy.
Clinical implementation of dynamic intensity-modulated radiotherapy: Dosimetric aspects and initial experience.
*J Med Phys*, 33(2):64–71, Apr 2008.

[31] Emiliano Spezi and D. Geraint Lewis.
Gamma histograms for radiotherapy plan evaluation.
*Radiother Oncol*, 79(2):224–230, May 2006.

[32] Markus Stock, Bernhard Kroupa, and Dietmar Georg.
Interpretation and evaluation of the gamma index and the gamma index angle for the verification of imrt hybrid plans.
*Phys Med Biol*, 50(3):399–411, Feb 2005.

[33] Markus Stock, Marlies Pasler, Wolfgang Birkfellner, Peter Homolka, Richard Poetter, and Dietmar Georg.
Image quality and stability of image-guided radiotherapy (igrt) devices: A comparative study.
*Radiother Oncol*, 93(1):1–7, Oct 2009.

[34] Bin S Teh, Arnold Paulino, and E. Brian Butler.
[recent developments in radiation oncology-integrating radiation physics and molecular radiobiology advances into clinical radiotherapy practice and beyond].
*Ai Zheng*, 27(8):885–893, Aug 2008.

[35] S. Webb.

Intensity-modulated radiation therapy (imrt): a clinical reality for cancer treatment, "any fool can understand this". the 2004 silvanus thompson memorial lecture.
*Br J Radiol*, 78 Spec No 2:S64–S72, 2005.

[36] Tilo Wiezorek, Tim Brachwitz, Dietmar Georg, Eyck Blank, Irina Fotina, Gregor Habl, Matthias Kretschmer, Gerd Lutters, Henning Salz, Kai Schubert, Daniela Wagner, and Thomas G Wendt.
Rotational imrt techniques compared to fixed gantry imrt and tomotherapy: multi-institutional planning study for head-and-neck cases.
*Radiat Oncol*, 6(1):20, 2011.

[37] Sua Yoo and Fang-Fang Yin.
Dosimetric feasibility of cone-beam ct-based treatment planning compared to ct-based treatment planning.
*Int J Radiat Oncol Biol Phys*, 66(5):1553–1561, Dec 2006.

[38] C. X. Yu.
Intensity-modulated arc therapy with dynamic multileaf collimation: an alternative to tomotherapy.
*Phys Med Biol*, 40(9):1435–1449, Sep 1995.

[39] Cedric X Yu and Grace Tang.
Intensity-modulated arc therapy: principles, technologies and clinical implementation.
*Phys Med Biol*, 56(5):R31–R54, Mar 2011.